

SCANNING TRANSMISSION ELECTRON MICROSCOPY: AN EXPERIMENTAL TOOL FOR ATOMIC SCALE INTERFACE SCIENCE

N. D. Browning¹, E. M. James¹, K. Kishida¹, I. Arslan¹, J. P. Buban¹, J. A. Zaborac¹,
S. J. Pennycook², Y. Xin^{1,2} and G. Duscher^{1,2*}

¹Department of Physics (M/C 273), University of Illinois at Chicago, 845 West Taylor Street, Chicago, IL 60607-7059. USA.

²Solid State Division, Oak Ridge National Laboratory, P.O. Box 2008, Oak Ridge, TN 37831-6030. USA.

* Current address: Department of Physics and Astronomy, Vanderbilt University, Nashville, TN, USA

Received: October 30, 1999

Abstract. Although internal interfaces have long been known to dominate the performance of many materials systems critical to modern technology, there has yet been little incontrovertible evidence pointing to the fundamental origin of the structure-property relationships. However, the recent development of direct imaging and analysis techniques in the scanning transmission electron microscope (STEM) has provided a new experimental pathway to obtain information on the local atomic structure, chemical composition and bonding at interfaces on the fundamental atomic scale. This is precisely the information that is required to unravel the complexities of interfaces and opens up a new paradigm for investigating the structure-property relationships at internal interfaces. In this paper we discuss the practical aspects of the experimental STEM techniques and demonstrate the resolution possible in current commercially available instrumentation. The application of these techniques to the study of internal interfaces is highlighted by a discussion of the analysis of homophase interfaces in SrTiO₃, Bi₂Sr₂Ca₂Cu₃O₁₀ and YBa₂Cu₃O_{7.8} and the heterophase interfaces between GaAs and Au, and between Si and molecular beam epitaxy (MBE) grown II-VI semiconductors.

1. INTRODUCTION

Internal interfaces have long been known to be the key to many mechanical and electrical properties [1,2]. Extensive microstructural evaluations have been performed recently on for example, metal-oxide interfaces [3-5], semiconductor-oxide interfaces [6,7], semiconductor-metal interfaces [8,9] and grain boundaries [10-14] important for a wide variety of technological applications. In many cases, the length scale over which the analysis was performed depends on the particular property that was being tested for, and more often than not, the availability of high-spatial resolution instrumentation. Obviously, the study of interfaces is a huge field and we cannot hope to cover it all here. In this paper, therefore, we concentrate on the analysis of interfaces where understanding the complexities of the structure-property relationships requires fundamental atomic scale information. In particular, we will describe the requirements for the instrumentation to obtain the atomic scale information and will focus on the recently developed incoherent Z-contrast imaging [15] and electron energy loss spectroscopy (EELS) [16] techniques in the scanning transmission electron microscope

(STEM). Furthermore, we will describe the use of basic theoretical models to correlate multiple imaging and analytical techniques together and finally, present some examples demonstrating materials interface problems where these techniques have provided fundamental atomic scale information on the structure-property relationships.

2. EXPERIMENTAL TECHNIQUES

The key to high-resolution STEM is the formation of an electron probe of atomic dimensions. Fig. 1 shows a schematic of the experimental microscope conditions and the relationship between the probe, the specimen and the various detectors that we will be discussing in the upcoming sections. Essentially, whether we consider a dedicated STEM [17] or one of the more modern TEM/STEM instruments [18], the electron optics of the microscope above the specimen are aligned in such a way as to make the probe as small as possible on the surface of the specimen. For a given acceleration voltage the size of the probe is dependent on the spherical aberration coefficient of the probe forming lens. As the general principles of aligning and optimizing the

Corresponding author: Prof. Nigel D. Browning, e-mail: Browning@uic.edu

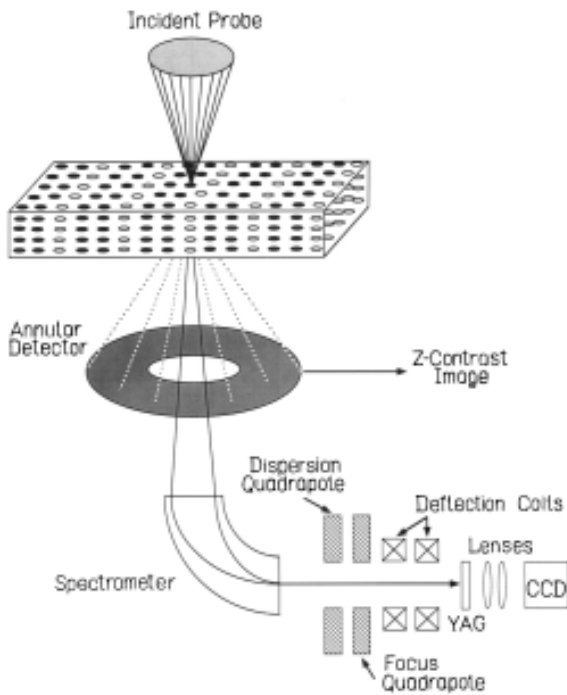


Fig. 1. Schematic of the detector geometry for a general STEM.

probe are the same for all STEMs we only discuss here the specifics of probe formation in the JEOL 2010F TEM/STEM as an example of how the process works experimentally [18, 19].

Fig. 2 shows the electron optical arrangement of the probe-forming system in the JEOL JEM-2010F. The de-magnification of the Schottky field emission source in this microscope is achieved by an electrostatic gun lens and a twin condenser lens system. One difference compared to the cold field emitter generally used in dedicated STEM, is that the Schottky electron source has a much larger emission area. Each element of the source is assumed to emit incoherently and therefore leads to an incoherent broadening of the probe. However, this is overcome by a large de-magnification factor between source and probe. The drawback in terms of instrument performance is that this is at the expense of decreasing the amount of current in the probe. In particular, by using the C1 lens near maximum excitation, a cross-over is formed between the two condensers and a large source de-magnification can then be achieved (probably a factor of ten greater than is necessary in the cold field emission STEM). C2 and the gun lens can then be used to tune the probe coherence further, depending on the probe size that is required.

This tuning and optimizing of the electron probe can be achieved most readily with the electron “Ronchigram”, or “shadow image”. This is because

the intensity, formed at the microscope Fraunhofer diffraction plane, varies considerably with angle, and this variation is a very sensitive function of lens aberrations and defocus [20, 21]. When the excitation of each illumination electron optical component (i.e. lens, stigmator) is slightly changed, very small misalignments become apparent by translations in the pattern that depart from circular symmetry. Furthermore, the presence or absence of interference fringes in the pattern indicates the amount of incoherent probe broadening due to instabilities and the effect of a finite source size. Fig. 3 shows schematically the ray diagram for Ronchigram formation. The probe remains stationary and the post-specimen intensity is recorded as a function of angle by a CCD camera or equivalent device.

Typical Ronchigrams at the amorphous edge of a specimen are shown in Fig. 4. At large defocus, the electron cross-over is at a relatively large distance from the specimen, and a projection image is observed. As Gaussian focus is approached, an angular dependence to the magnification emerges, due to lens aberrations and the manner in which they change the phase of the electron beam. At slight underfocus, the azimuthal and radial circles of infinite magnification can be seen [21]. These are the angles at which defocus and spherical aberration effectively cancel and are characteristic of Ronchigrams from a round, probe-forming lens. Axial astigmatism can be very accurately corrected by exciting the stigmator coils so that these Ronchigram features are circularly symmetric. As the beam is focused, the central, low angles display the highest magnification. The coma free axis is clearly defined by this position and all alignment and positioning of detectors and apertures can be performed with respect to this spot. The prime advantage of using a Ronchigram is that the coma-free axis is directly visible. In other alignment methods, the current or voltage center of the objective lens must be used as the reference and this is not always sufficiently accurate. Next, the illumination beam alignment can be very accurately checked by wobbling first the condenser lens excitation and then the microscope high tension. If there is a misalignment of the beam between condenser and objective lenses, there will be a periodic translation of Ronchigram features as the wobbling takes place. This can be corrected using the condenser alignment coils so that the features only oscillate in and out about the coma-free axis [22-24].

The probe has now been aligned with respect to the coma-free axis. Control of its intensity distribution is now dependant on the exact illumination lens settings and the size of the STEM objective aperture that is subsequently inserted to exclude aberrated beams at high

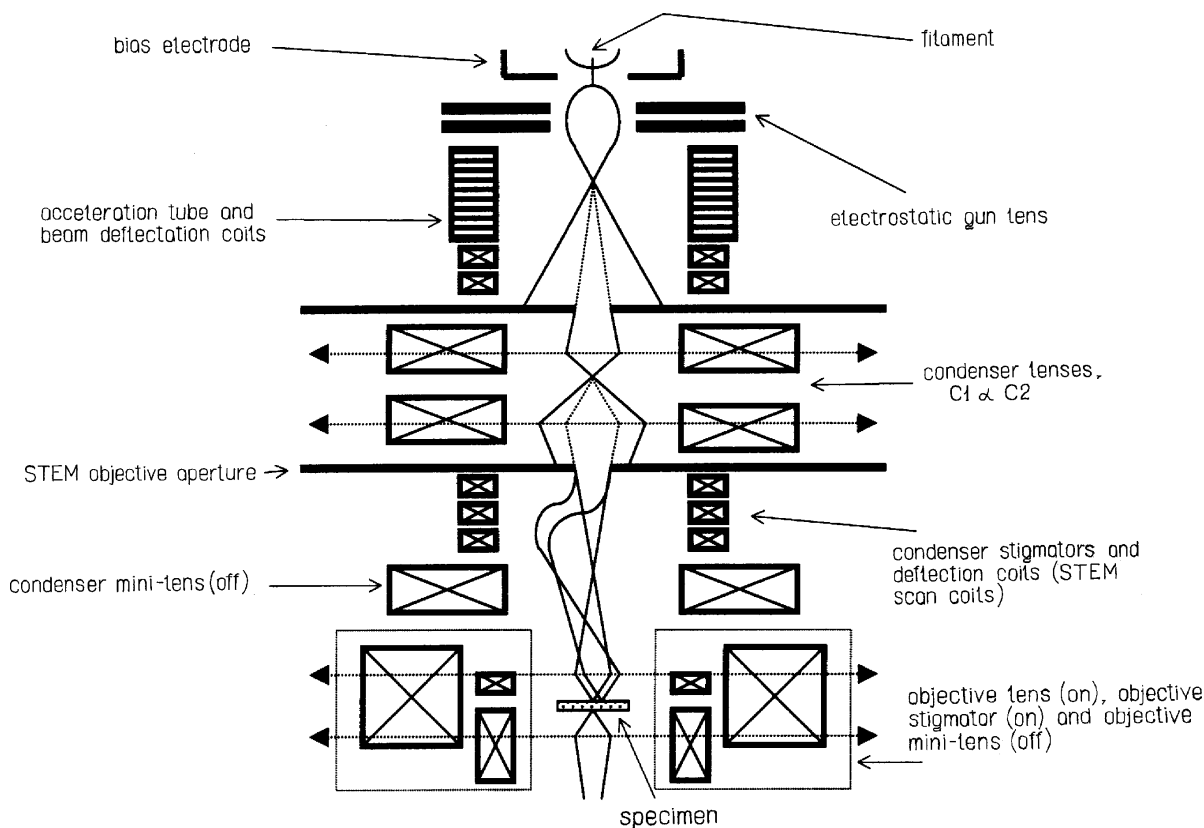


Fig. 2. Schematic of the probe forming optics in the JEOL 2010F STEM.

angles. Fig. 5 shows Ronchigrams from a thin region of Si $\langle 110 \rangle$ at slight defoci. Diffraction effects are clearly present in the pattern and lattice fringes are observed if the probe coherence is great enough. Also, at large defocus, when a shadow image at low magnification is visible, the crystal Kikuchi lines are seen (Fig. 5). Since the coma-free axis position is already known, it is simple to adjust the specimen tilt so that the desired zone axis is aligned precisely, for the sub-micron specimen area that is of interest in the experiment. The microscope and the specimen are now in precisely the optimum conditions to perform experiments at the highest spatial resolution available. It is now only necessary to define the type of scattered signal that will be collected as a function of the probe position to form the experimental image.

2.1. Z-contrast imaging

Z-contrast images [14,15,17] are formed by collecting the high-angle scattering (40-100 mrad at 200 kV [18]) on an annular detector (Fig. 1). Detecting the scattered intensity at these high-angles and integrating over a large angular range effectively averages coherence effects between neighboring atomic columns in the specimen. Thermal vibrations reduce the coherence between atoms in the same column to residual correlations between near neighbors [25,26], a second order effect.

This allows each atom to be considered as an independent scatterer. Scattering factors may be replaced by cross sections, and these approach a Z^2 dependence on atomic number. This cross section effectively forms an object function that is strongly peaked at the atom sites, so for very thin specimens where there is no dynamical diffraction, the detected intensity consists of a convolution of this object function with the probe intensity profile (Fig. 6) [17]. The small width of the object function (~ 0.02 nm) means that the spatial resolution is limited only by the probe size of the microscope (the optimization of which is achieved using the Ronchigram, as described above). For a crystalline material in a zone-axis orientation, where the atomic spacing is greater than the probe size, the atomic columns are illuminated sequentially as the probe is scanned over the specimen. An atomic resolution compositional map is thus generated, in which the intensity depends on the average atomic number of the atoms in the columns.

This result also holds true for thicker specimens. It has previously been noted that for specimens in zone-axis orientations, the STEM probe forms narrow spikes around the atomic columns as it propagates [27]. This effect is caused by the coherent nature and large angular spread of the STEM probe, which leads to the tightly bound s -type Bloch states adding constructively and

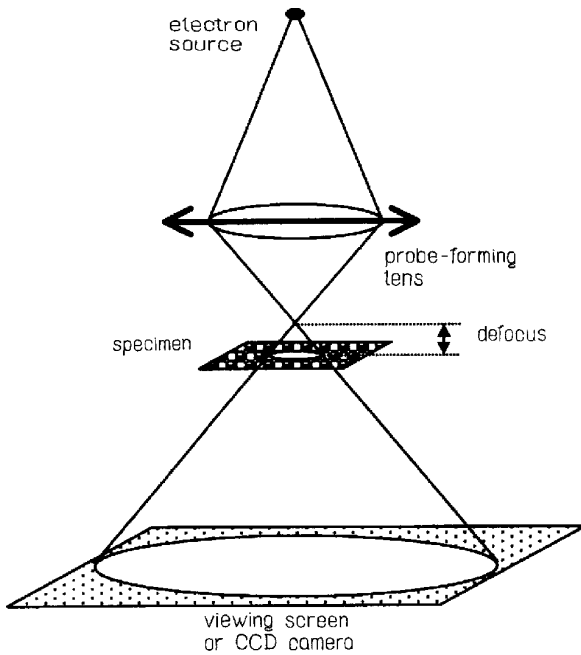


Fig. 3. Simplified ray diagram showing the formation of an electron Ronchigram.

the less localized states interfering destructively [17]. This effect is enhanced for scattering processes such as high-angle thermal diffuse scattering that are localized at the atomic cores, causing a great reduction in beam broadening. With only one dominant Bloch state, dynamical diffraction effects are largely removed and manifest only as a columnar channeling effect, thus maintaining the thin specimen description of the image as a simple convolution of the probe intensity profile and an object function, strongly peaked at the atom sites (Fig. 6).

The phase problem associated with the interpretation of conventional high-resolution TEM images is therefore eliminated. In thin specimens, the dominant contribution to the intensity of a column is always its composition, although due to the higher absorption of the heavy strings the contrast does decrease with increasing specimen thickness and in very thick crystals there is no longer a high resolution image. The effect of changing focus is also intuitively understandable as the focus control alters the probe intensity profile on the surface of the specimen. For defocus less than the optimum Scherzer condition, the probe broadens causing the individual columns not to be resolved. For higher defocus values the probe narrows with the formation of more intense tails, causing sharper image features but compositional averaging over several columns. The optimum focus condition therefore represents a compromise between high resolution (narrow probe profile) and the desire for a highly local image (no significant tails to the probe). This also

corresponds to the optimum probe for microanalysis [16, 28, 29].

At defects and interfaces, structures can become extremely complicated, causing difficulties in determining the precise 3-dimensional composition. However, provided an atomic column is continuous through the crystal, reconstructions will only result in a change in column intensity and not a contrast reversal [14]. The atomic structure in the region of defects and interfaces can therefore still be determined largely from the image, and used to position the electron probe for EELS [16, 28, 29].

2.2. Electron energy loss spectroscopy (eels)

As can be seen from Fig. 1, the annular detector used for Z -contrast imaging does not interfere with the low-angle scattering used for EELS [30]. This means that the Z -contrast image can be used to position the electron probe over a particular structural feature for acquisition of a spectrum [16, 28, 29]. The physical principle behind EELS relates to the interaction of the fast electron with the sample to cause either collective excitations of electrons in the conduction band, or discrete transitions between atomic energy levels, e. g. $1s \rightarrow 2p$ transitions [30]. The ability to observe discrete atomic transitions allows compositional analysis to be performed by EELS (the transitions occur at characteristic energy losses for a given element). Furthermore, the transitions to unoccupied states above the Fermi level allows the degree of hybridization between atomic orbitals to be determined, i.e. information on local electronic structure (bonding) changes can be ascertained.

To be able to correlate the spectrum precisely with the structural feature seen in the image, it is essential that the spectrum have the same atomic resolution as the Z -contrast image. In order to achieve this atomic resolution, the range over which a fast electron can cause an excitation event must be less than the inter-atomic spacing. Hydrogenic models [31,32] show that for the majority of edges accessible by conventional energy-loss spectrometers ($\Delta E < 2$ keV) the object functions are localized within 0.1 nm of the atom cores [33-35]. Hence, like the Z -contrast image, we have an object function localized at the atom cores and an experimental probe of atomic dimensions. For crystalline materials in zone-axis orientations, providing we maintain a large collection angle (15-30 mrad), coherent effects will be averaged and the description of the spectrum in terms of a convolution of the probe with an object function is valid (Fig. 6). An important aspect of this experimental approach is that the probe channeling discussed for Z -contrast imaging will also preserve the spatial resolution of the spectrum, thereby

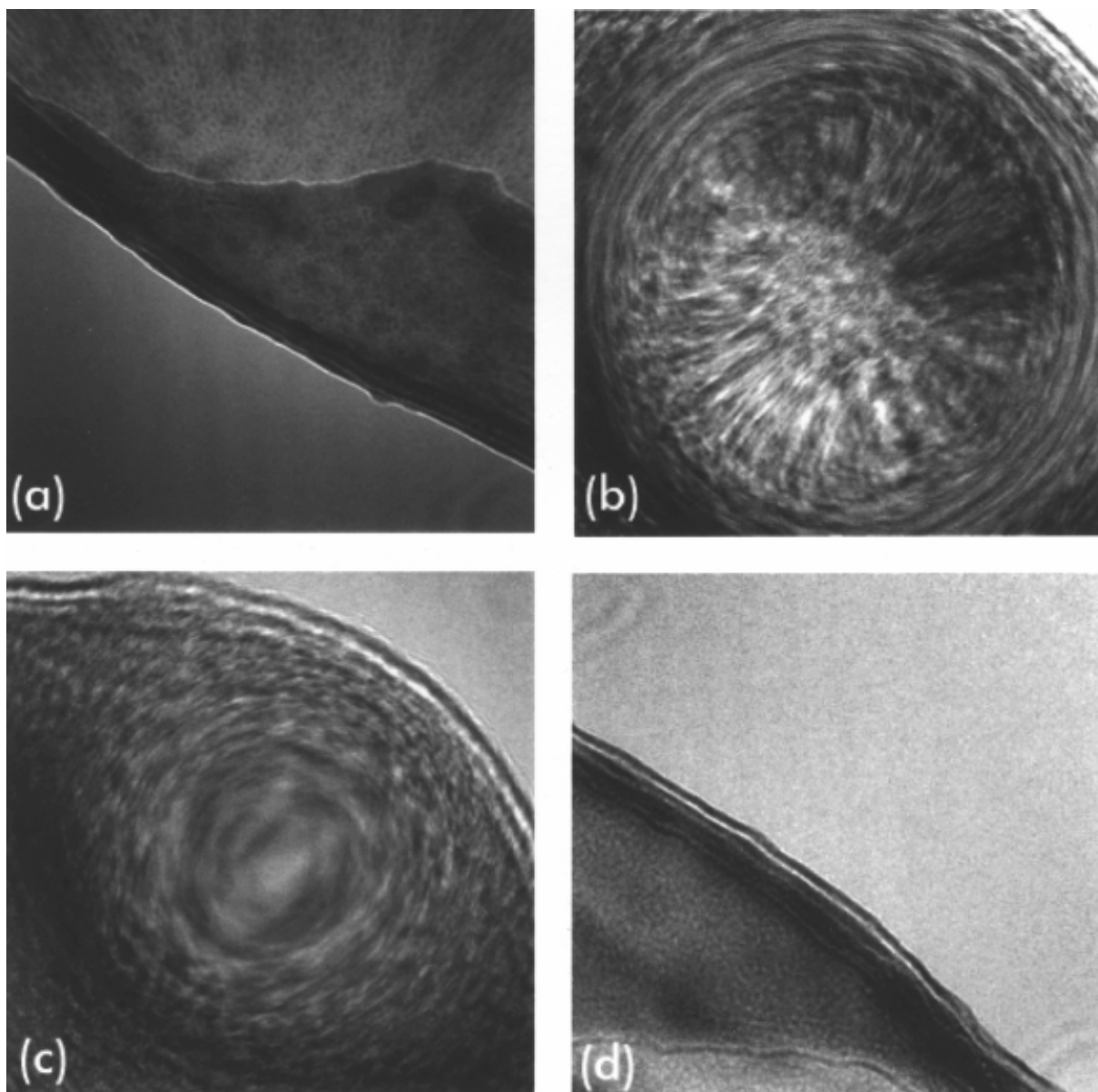


Fig. 4. Experimental electron Ronchigrams of a thin amorphous carbon layer. (a) large underfocus — Rays at all angles cross the optic axis after the specimen and a shadow image of the specimen edge is seen. (b) small underfocus — Low angle rays cross the optic axis after the specimen. High angle rays cross before the specimen, because of the effect of spherical aberration. The shadow image therefore changes in magnification as a function of angle and critical angles occur where there is infinite radial and azimuthal magnification. Departures from circular symmetry indicate the presence of astigmatism. (c) Gaussian focus — The lowest angle rays cross the axis at the specimen; higher angle rays cross before it, due to the effect of spherical aberration. (d) overfocus — Rays at all angles cross the axis before the specimen and shadow image of the specimen edge is visible.

allowing atomic resolution analysis of the electronic structure to be achieved even with large collection apertures. Of course specimen drift is also a problem, but for the acquisition times of less than 5 s used in all practical applications discussed here, the $1\text{\AA}/\text{minute}$ drift of the microscope does not induce a significant broadening effect.

2.3. Interpreting the atomic resolution results

The combination of Z-contrast imaging and EELS allows us to obtain precise information on the atomic structure, chemical composition and electronic struc-

ture at interfaces and defects on the atomic scale. However, having obtained this wealth of information, the question remains as to how to incorporate it into a model for the interface that will allow us to understand the structure-property relationships. There are many theoretical methodologies that can be used to understand the structure-property relationships, ranging in complexity from *ab-initio* calculations [36] to empirical pair potentials that have their origins in crystal chemistry [37]. Although we acknowledge here that the optimum analysis of interfaces requires the

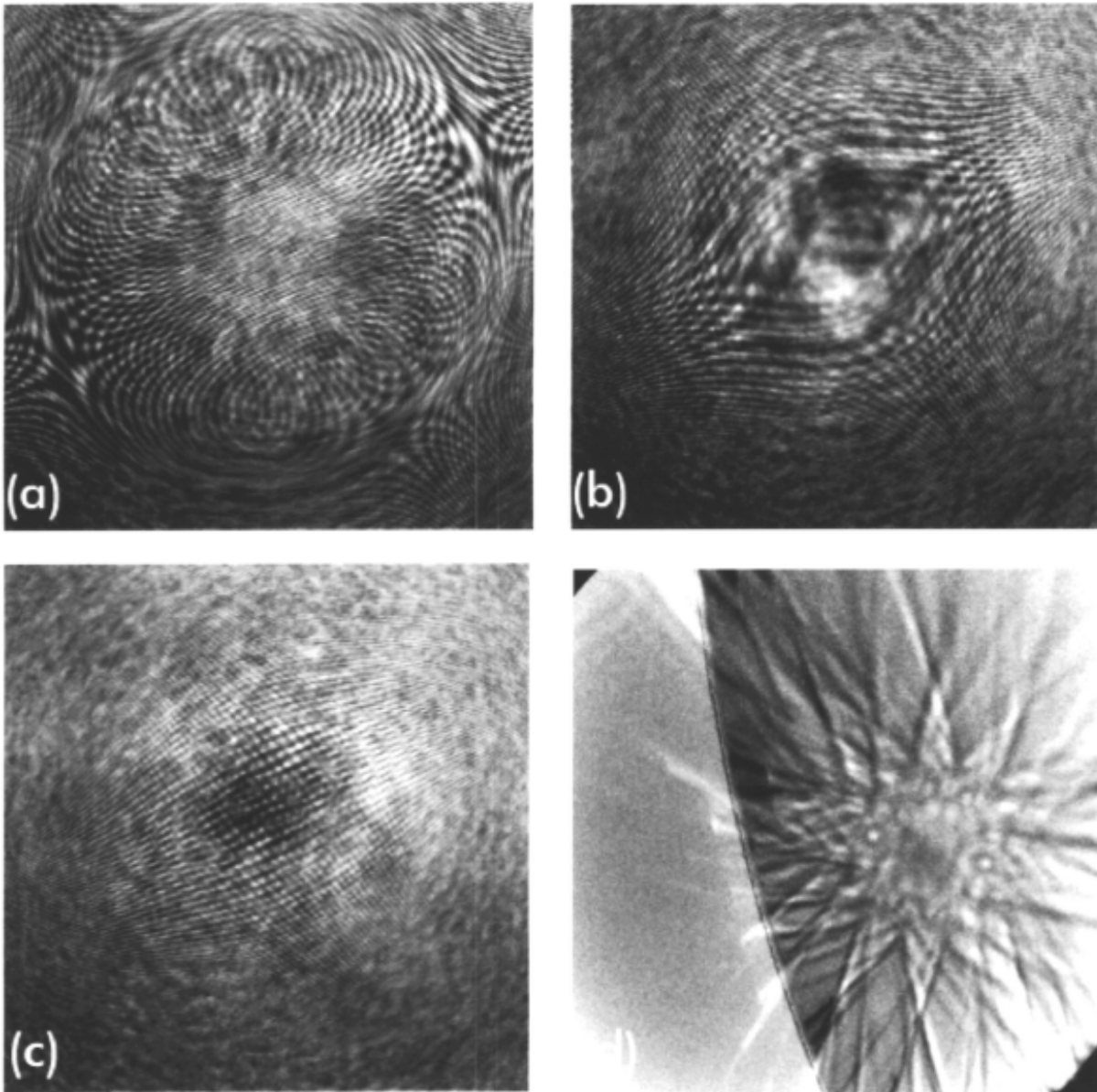


Fig. 5. Ronchigrams of a thin region of silicon $\langle 110 \rangle$ showing diffraction effects and fringes arising from the specimen periodicities. Visibility of the characteristic fringes depends on precise tilting of the specimen and the amount of probe coherence in a direction perpendicular to the relevant crystal lattice plane. (a) small underfocus – Lattice fringes are visible near the Ronchigram center and they become heavily distorted further out in angle. The distortion is due to phase changes introduced by the lens spherical aberration. (b) near Scherzer focus – The central fringes become large and wide. Their area corresponds to the entire overlap region between zero-order and relevant diffracted beams. (c) slight overfocus – Fringes are visible with size and spacing that decreases with increasing angle from the Ronchigram center. (d) the probe is well overfocused showing the Kikuchi lines.

use of *ab-initio* calculations, we will only discuss the more simple pair potentials and their application to the materials problems described in later sections. The reason for doing this is that, although the models provide only approximate solutions, the pair potentials allow us to deal with very general boundary structures, and the approximations at least allow us to capture the basics of the physical processes occurring at the interfaces being examined.

2.3.1. Simple Structural Models

The aim of the analyses described later in this paper is to determine the complete three-dimensional structure of an interface and to use this to infer the structure-property relationships. Hence, what is required in the initial stages is a simple means of verifying that the number of atoms and approximate structure observed in the Z-contrast image of the interface is correct. One means to do this is through combined distance least

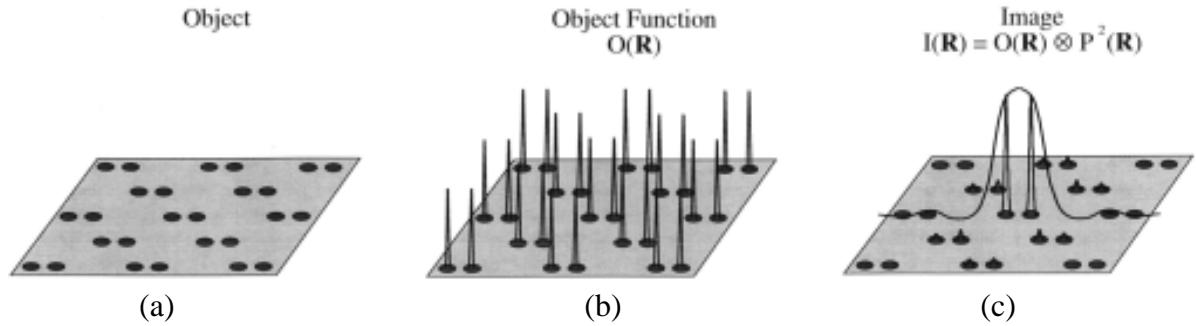


Fig. 6. The specimen consists of an array of atomic columns (a) for which the potential for high-angle scattering can be represented by an object function (b). The experimental image can be interpreted as a simple convolution of the experimental probe and the object function (c).

squares and bond-valence sum analysis of the Z-contrast image [38]. This distance-valence least squares analysis (DVLS) is based on a concept that was originally proposed by Pauling [37]. In Pauling's rules for crystal chemistry, it is assumed that the formal valence state of a given atom is composed of contributions from all the nearest neighbors. Additionally, the contribution to the valence from each of the neighbors should be as uniform as possible, i.e. the contributions to the formal valence state of an atom are shared equally between the nearest neighbors. These ideas have been further developed by Altermatt and Brown [39,40]. In a systematic study of crystal structures they find that the contribution of a single bond to the formal valence-state of the atoms involved follows the empirical relationship

$$S = \exp[(r_{ij} - r_0) / B], \quad (1)$$

where r_{ij} is the bond-length, r_0 is an equilibrium value for each atom pair and B is a constant (≈ 0.37).

While this relationship is determined only for perfect crystal structures, there is every reason to believe that the same basic principles will apply for interfaces. (We know that the structure exists as we have an image, and if the same elements are involved it is reasonable to assume their bonding will be similar). It is therefore possible to utilize this very simple pair potential between two atoms to check if the atoms in a proposed boundary structure are in a reasonable environment [14]. If the valence is too high, the bond length is too short and vice-versa. Furthermore, the equilibration of the bonds to the nearest neighbors using the distance least squares aspect of this formulation effectively forms a very basic energy minimization of the structure. Although such a minimization is by no means as accurate as *ab-initio* calculations, a benefit of this simple approach is that it requires minimal

computation capacity and within the errors ($\sim 10\%$), can verify that the number of atoms and their positions in the structure are physically reasonable [14,38].

2.3.2. Multiple Scattering Simulations

Having defined the numbers of atoms and their positions taken from the image to be physically reasonable with the bond-valence program, we are now in a position to use these positions to simulate the energy loss spectrum. As we know the atomic location from which the spectrum was acquired, we can construct atomic clusters from defined locations in the interface and use them to simulate the spectrum with multiple scattering analysis [41-44]. Although multiple scattering theory was originally developed for the analysis of X-ray absorption spectra, its application to EELS is straightforward [45] (only the method of excitation has changed from an X-ray to an electron). Multiple scattering calculations model the density of unoccupied states by considering the scattering of the photoelectron created during the excitation process, from neighboring atoms. The many paths which may be taken by a photoelectron alter the matrix elements for a particular transition due to constructive or destructive interference which occurs between the outgoing and returning photoelectron wave (Fig. 7). In effect, the resultant energy loss spectrum may be described as a simple absorption edge of hydrogenic form, due to an isolated atom, with intensity modulations due to the atomic structure of the solid (Fig. 7), i.e. the absorption $\alpha(E)$ is given by

$$\alpha(E) = \alpha_0(E) \left[1 + \sum_{n=2} X_n(E) \right], \quad (2)$$

where $\alpha_0(E)$ is the atomic absorption and $X_n(E)$ is the multiple scattering signal of order n ($n > 1$) which contains all the structural information [46]. Since this

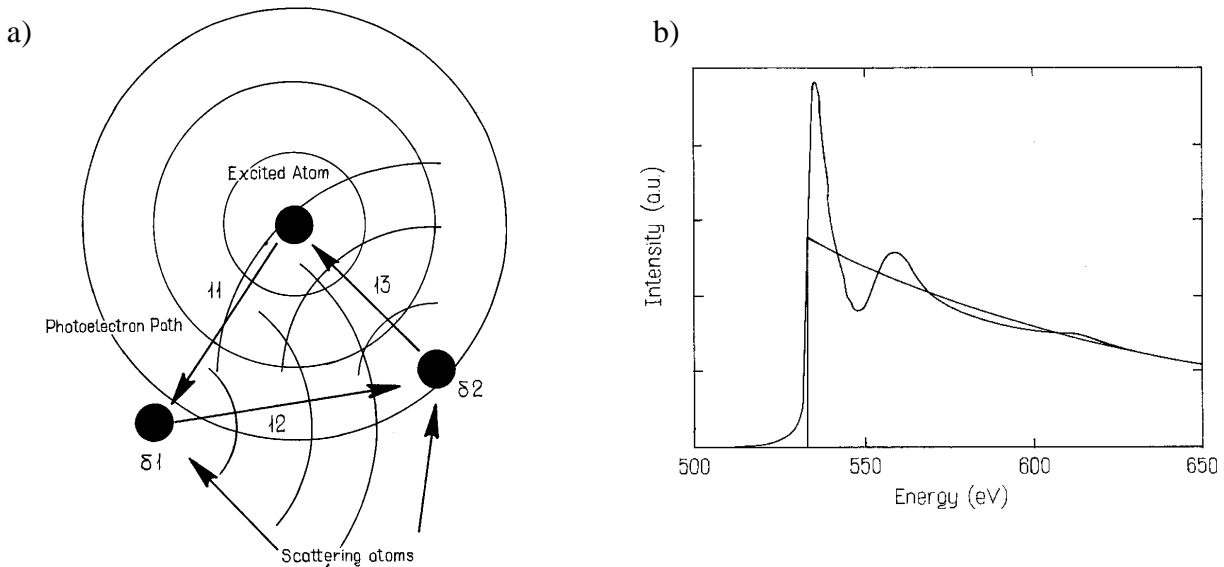


Fig. 7. (a) Multiple scattering calculations model the density of unoccupied states by considering the scattering of the excited photoelectron from neighboring atoms. The resultant energy loss spectrum may be described as a simple absorption edge of hydrogenic form, due to an isolated atom, with intensity modulations due to the atomic structure of the solid (b).

description of the unoccupied density of states is based on a real space cluster of atoms, several unique opportunities are presented for the analysis of interfaces. First of all, a lack of symmetry does not seriously affect the calculation, so as with the bond-valence analysis we can deal with very general interface structures. Additionally, the effects of dopant atoms may be simply investigated by substituting atom types within the cluster and recalculating the scattering. Multiple scattering therefore allows spectral changes to be directly interpreted in terms of structural changes. As we have a starting structural model for interfaces in the Z-contrast image (refined by bond-valence), with this multiple scattering analysis we can incorporate the third dimension and any compositional changes into complete models on which to base the interpretation of the structure-property relationships.

2.4. Application of STEM techniques to materials problems

One of the main principles behind the use of the STEM to solve interface problems is that the analytical and imaging techniques can be correlated together with atomic resolution (using in the most simple case bond-valence and multiple scattering analysis to achieve the correlation). This provides extra information that allows us to investigate the very complex structural and chemical behavior that can occur. As an example of the use of correlated techniques and basic interpretation tools described above to investigate atomic scale phenomena, we describe here the analysis of edge dislocations in metal-organic vapor phase epitaxy

(MOVPE) grown GaN thin films [47]. These structures are of fundamental interest to the materials science community, as a high density of threading dislocations appears to have a benign effect on GaN high efficiency light emitting diodes. The origin of the benign effect remains unclear as although early work [48, 49] suggested that threading dislocations are not non-radiative recombination centers, the increase in optical properties that is achieved [50] by reducing the threading dislocation density in the epitaxial lateral overgrowth method [51], provides circumstantial evidence that dislocations do in fact have a deleterious effect. Furthermore, recent more direct evidence indicates that threading dislocations can be optically and electrically active [52-59].

Fig. 8 shows a Z-contrast image obtained from the VG HB603 U dedicated STEM (the alignment, operation and resolution of which is the same as the JEOL 2010F described in earlier sections. The only difference being that this instrument has a cold field emission gun). The core clearly shows the eight-fold ring structure, as previously reported [60]. On the basis of the prior theoretical calculations, this n-type sample grown under N-rich growth conditions (The sample is also doped with Si at a level of $\sim 2 \cdot 10^{18} \text{ cm}^{-3}$ and has a free carrier mobility is about $200 \text{ cm}^2/\text{Vs}$) is expected to show a Ga-vacancy core structure [54]. Since atoms contribute to the image according to their mean square atomic number (Z), the light N atoms contribute only 5% of the image contrast in a full GaN atomic column. Thus it is immediately apparent from the image that the Ga vacancy concentration must be much less than

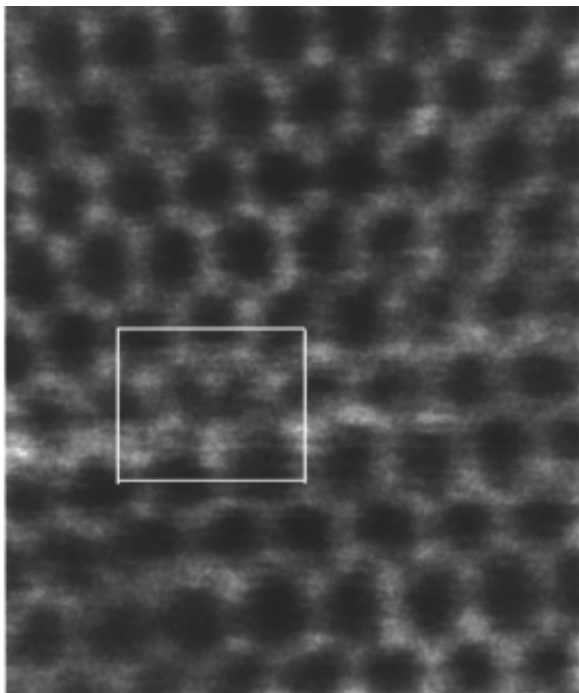


Fig. 8. Z-contrast image of a pure edge dislocation core obtained with 0.13 nm resolution in the VG Microscopes HB603 U.

100%. At the typical thicknesses used for Z-contrast imaging, the image intensity is roughly proportional to the number of atoms in a column [17]. Therefore our sensitivity to Ga vacancies is limited just by the statistical variations in column intensities close to the dislocation core. Integrated columnar intensities showed a mean deviation of 15%. From this data we therefore estimate the Ga vacancy concentration to lie in the range 0-15% per *c*-axis repeat, which implies a significantly lower line charge than previously assumed for threading dislocations in GaN.

The local electronic structure in the core can be investigated using the Nitrogen K-edge EELS spectrum. This absorption edge gives information on transitions from the 1s core level to the unoccupied density of states in the conduction band with 2p symmetry. Fig. 9 shows the dislocation image obtained from the 2010F with the larger beam diameter used for EELS (For spectroscopy, the probe size is increased from the 0.14nm resolution limit to 0.2nm in order to provide more signal). Fig. 9 also shows experimental nitrogen K-edge spectra obtained from several pure edge dislocation cores as well as from nearby perfect regions of the film for comparison. Each spectrum is the summation of 13 spectra from 8 dislocation cores with an acquisition time of 5 seconds for each individual spectrum and with an energy dispersion of 0.2eV/channel. The experimental collection conditions (see earlier sections) result in an energy resolution of 1.2eV. A power-

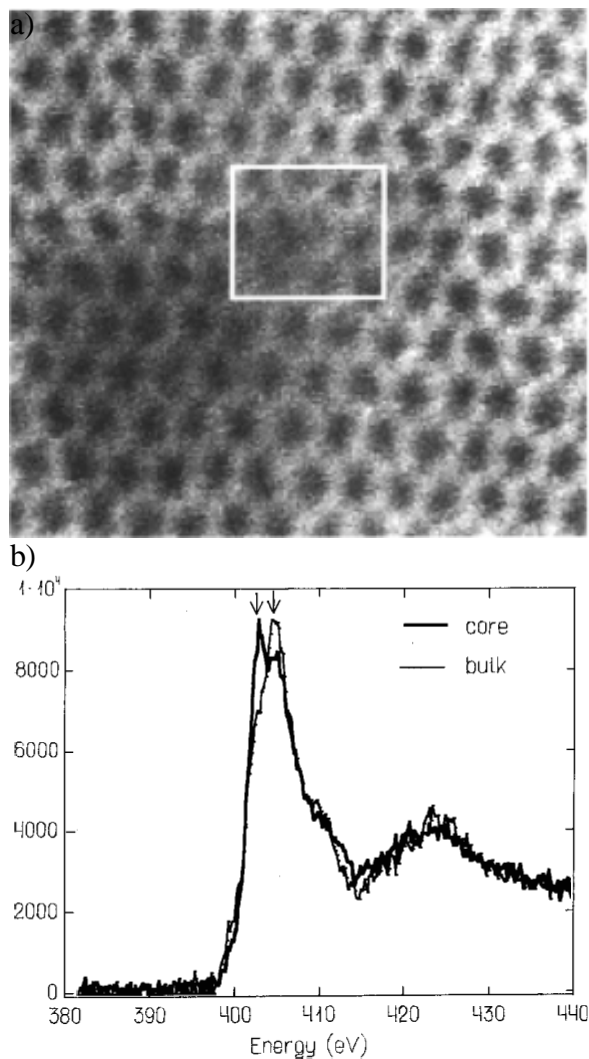


Fig. 9. (a) Z-contrast image of the pure edge dislocation core with a 0.2 nm beam in the JEOL 2010F to give sufficient current for (b) the experimental EELS spectra obtained from the core column.

law background subtraction has been used [30], but otherwise the spectra are as acquired.

It can be clearly seen that there are dramatic changes in the fine structure of the Nitrogen K-edge spectra on and off the dislocation core. In particular, in the core spectrum, the first peak 2.2eV above edge onset (398eV) rises significantly relative to the second peak. Simulations of the electronic structure using the multiple scattering methodology of the FEFF 8 [43] codes described in earlier sections of this paper are also shown in Fig. 10 (the clusters were built using the bond valence analysis also described earlier). These simulations take full account of the experimental conditions in the relative weighting of the in-plane and *c*-axis component of the experimental spectrum [61] and show a similar trend to the experimental results. The increase in absorption just beyond the band gap is most likely due to the broken symmetry in the region of the core [62].

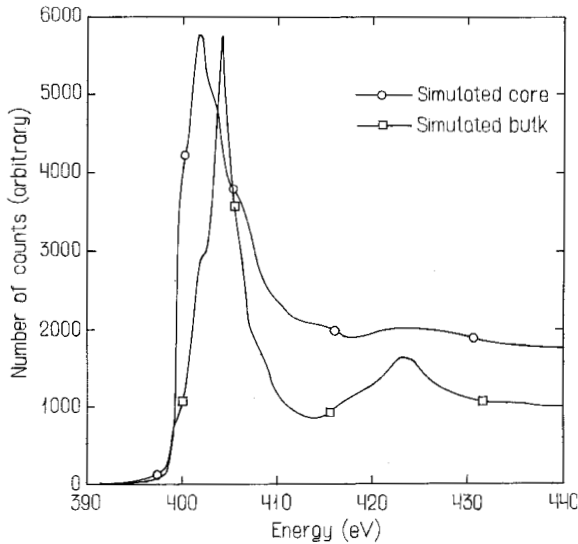


Fig. 10. Multiple scattering simulations of the experimental GaN bulk and core spectra showing that the main features in the spectra can be reproduced by considering clusters containing no vacancies.

The combination of the Z-contrast image and EELS therefore provides significant information on the local atomic and electronic structure changes at the dislocation core. In particular, it is noteworthy that no absorption is seen in the region of the band gap. This is consistent with any Ga vacancy induced acceptor states being full, as expected if the dislocation line is charged. However, the Z-contrast image suggests that the vacancy concentrations in the core may be less than previously considered, which may explain the benign effect of threading dislocations on the electrical and optical properties. However, a full understanding of this subtlety requires extensive investigation by *ab-initio* methods, which are currently underway. We must, of course, also consider the effect of screw dislocations and mixed dislocations in attempting to draw definitive conclusions between the structure of dislocations and the bulk properties of the film. Here our intention is simply to point out that the experimental tools to make such measurements now exist.

3. HOMOPHASE INTERFACES

The first set of interface problems that we describe relates to homophase interfaces, or grain boundaries. In this set of problems, the material a distance of ~ 1 nm either side of the interface can be described as being bulk like in structure. Our aim in performing the atomic resolution STEM analysis is to understand the relationship between structure and properties in this 1-2 unit cell region at and around the grain boundary plane.

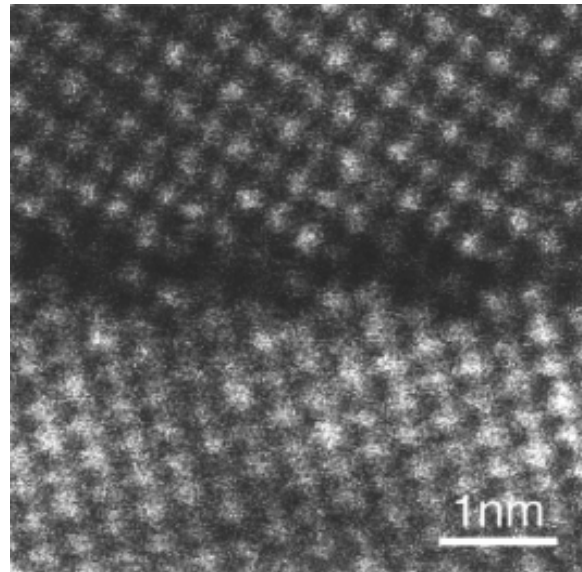


Fig. 11. Z-contrast image of a 36° [001] tilt grain boundary in SrTiO_3 .

3.1. SrTiO_3

SrTiO_3 has been the subject of many recent investigations. Although each of the individual investigations had specific reasons, the wealth of information that is available on SrTiO_3 is really due to its existence as the most basic of perovskite materials [63]. However, unlike the perovskites being developed for high- T_c superconductors [64], ferroelectrics [65], novel dielectrics [66] and colossal magneto resistance materials [67], it shows none of the detailed electronic and ionic functions of those materials. For our purposes, this means it can be used to investigate some of the fundamental structures and processes that occur at grain boundaries in perovskites [14, 68, 69].

Fig. 11 shows a typical Z-contrast image obtained from a 36° [001] tilt grain boundary in SrTiO_3 (the image was obtained from a VG HB603 STEM). From analysis of this boundary and images from other symmetric and asymmetric [001] tilt boundaries [68,69] it can be seen that the boundary plane is composed of distinct repeating “structural units”. The structural unit model [1,70] for grain boundaries is formally equivalent to dislocation core models [71]. However, rather than characterizing the dislocations by a series of cores with defined Burgers vectors, the structural unit model focuses on the atomic arrangements within the core. This is of particular use for the study of oxide grain boundaries, where the atomic arrangement can lead to different bonding interactions between the metal and oxygen atoms. The structural units needed to construct

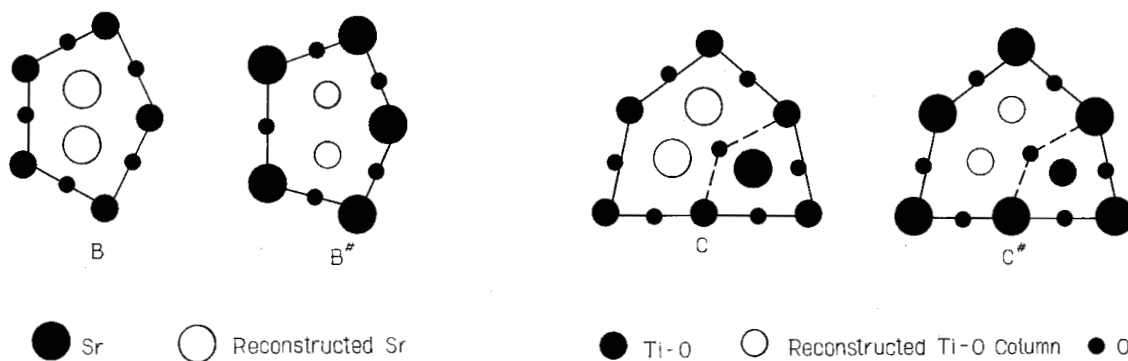


Fig. 12. Structural units for [001] tilt grain boundaries in SrTiO_3 . The B unit is equivalent to a (100) dislocation core and the C unit to a (110) dislocation core.

all [001] tilt grain boundaries in SrTiO_3 are shown in Fig. 12 [68,69].

As can be seen from Fig. 12, the structural units can be centered on either of the cation sub-lattices. This experimental observation of structural units on both the Sr and the Ti sub-lattices immediately highlights an advantage of this methodology in investigating the structure-property relationships of grain boundaries. The chemistry of the A and B sites in the perovskite structure (formula ABO_3) is different, and it can be expected that dislocation cores on the different sub-lattices will exhibit different chemical effects. This factor is not included in dislocation core models, where the only discriminating factor for each core is a Burgers vector that is independent of the atomic structure in the core. Furthermore, if we examine the structural units more closely, we see that there are locations where the columns appear too close together. In such situations, like-ion repulsion should preclude such a structure. However, if we remember that the Z-contrast image, like any transmission image, is simply a 2-D projection of the 3-D crystal structure, a solution to this problem is for only one of the two sites in each perovskite block in the c-direction to be occupied. We would still see two columns in projection, but avoid like-ion repulsion. An alternative view of these “half-columns” is that they are a single atomic column that is distorted through the thickness of the crystal in a regular manner, i.e. a 2×1 reconstruction.

To understand the effect of this 2×1 reconstruction on the electronic properties of the grain boundaries we can get further information from EELS. The oxygen K ionization edge and titanium $L_{2,3}$ ionization edge obtained from the grains and the boundary are shown in Fig. 13. As can be seen from the figure, there are still two peaks in the Ti $L_{2,3}$ edge and therefore the crystal field remains, and the Ti atoms at the boundary must still be octahedrally coordinated. There is also a reduction of the crystal field, which is explained simply by a distortion of this octahedral coordination. The

π^* maximum (1st peak) of the O- K ionization edge is lower at the grain boundary than in bulk while the σ^* maximum (2nd peak) is higher. These changes have been associated with the distortion of O-Ti-O bond angle [72] and is also consistent with behavior observed in TiO_2 [73]. To summarize, two features change at pristine grain boundaries: the distance of the first two peaks of the Ti- $L_{2,3}$ and the peak ratio of the first two peaks in the O- K edge. From these changes we can say that Ti remains basically octahedrally coordinated by O, but the distortion of the octahedra results in Ti-O bond angles deviating from 180° . These conclusions have been verified by bond-valence calculations and multiple scattering analysis of the 25° [001] tilt grain boundary structure [45].

Having defined the changes in both the atomic and electronic structure that occur at undoped or pristine grain boundaries, we are now in a position to evaluate how the incorporation of a dopant atom at the boundary affects the properties. In the case of acceptor like dopants, i.e. Fe^{3+} substituting for Ti^{4+} , there has been observed to be significant segregation of the acceptors at the boundary [74] and the occurrence of Schottky barrier-like transport behavior [75]. In this experiment, Mn acceptors were diffused into the grain boundary plane by annealing a 36° [001] tilt boundary bicrystal covered with MnO_2 paste at 1350°C in air for 5.5 hours. The Z-contrast image of this boundary, in Fig. 14, shows that there is no secondary phase formed at the boundary and the boundary itself has the same structural units as observed for the pristine boundary shown in Fig. 11 [29, 76].

Ti- $L_{2,3}$ edges were obtained while the beam was scanned in a rectangular area of about 1.5 unit cells (0.6nm–1.0 nm). The Ti- $L_{2,3}$ edges from the grain boundary core and bulk are shown in Fig. 15. Consistent with the pristine grain boundaries, the crystal field splitting is reduced, but the onset of the edge did not shift in energy. We can therefore conclude that the Ti atoms have the same distorted octahedral oxygen coordination

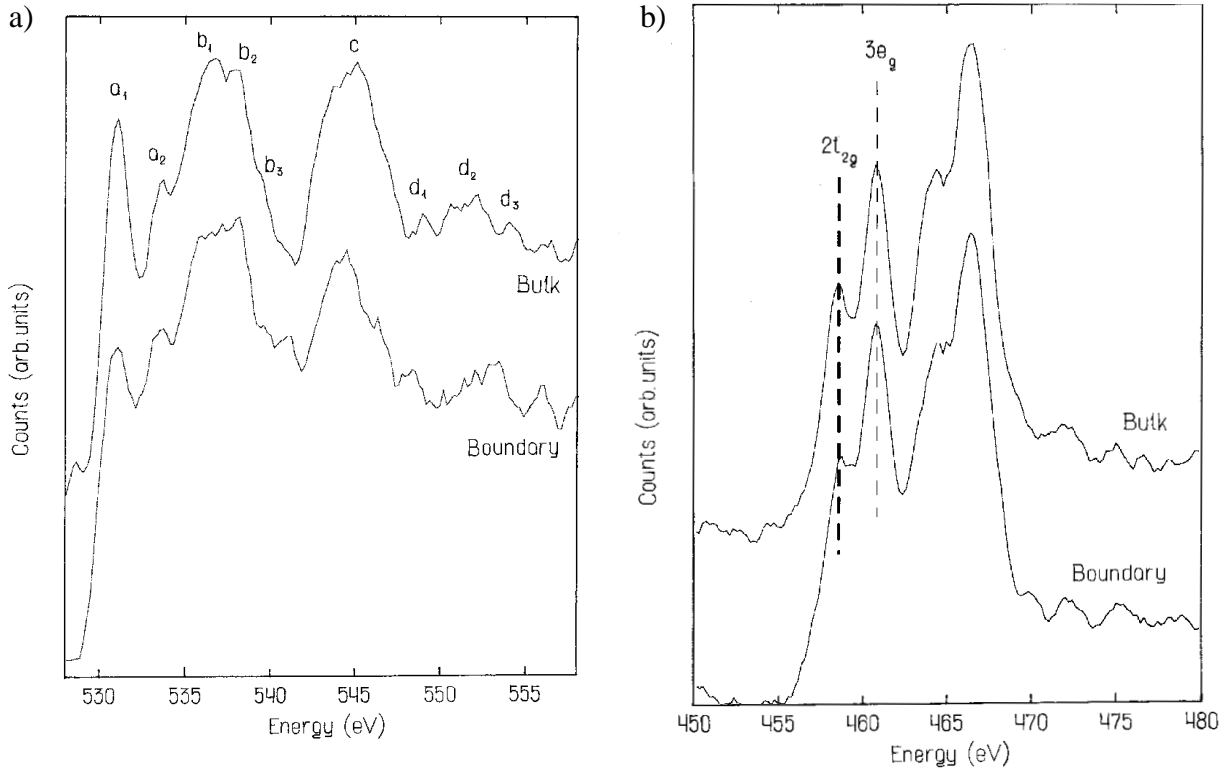


Fig. 13. (a) Oxygen K -edge and (b) titanium L -edge from the bulk and 25° [001] tilt grain boundary in SrTiO_3 . These spectra are taken to be representative of all undoped grain boundaries in SrTiO_3 due to the similarity of the structural units shown in Fig. 12.

at this boundary (this seems appropriate as the image shows the same structural units). A quantification and comparison of the $\text{Ti-}L_{2,3}$ ELNES with results from the pristine grain boundary is not possible due to differences in spatial and energy resolution.

Single atom column resolution was however obtained for the $\text{O-}K$ and $\text{Mn-}L_{2,3}$ edge. The numbers in Fig. 16 correlate with the positions the beam was located (see Fig. 14) while spectra were taken. The ELNES of the $\text{O-}K$ edge and the intensity of the $\text{Mn-}L_{2,3}$ edge can be seen to change dramatically from column to column. The maximum intensity of the $\text{Mn-}L_{2,3}$ edge coincides with the reconstructed Ti-O columns at the core of the dislocation unit [14, 68, 69]. This result is not surprising as Mn is expected to substitute for Ti . However, the Mn signal was also seen up to 2 nm away from the boundary. This distribution profile was to be expected from the way the sample was prepared; the Mn fast diffused along the grain boundary and then proceeded more slowly into the bulk.

To determine the oxidation state of Mn we performed an analysis of the $\text{Mn-}L_{2,3}$ near-edge fine structure. More than 90% of the $\text{Ti-}L_{2,3}$ ELNES are due to transitions between $2p$ and d symmetry conduction bands. In the following we will therefore ignore any contributions from $2p \rightarrow s$ transitions. We analyzed the ratio between the continuum (chosen to be represented

in the area between 20 to 40 eV after the onset) and the sum of the L_3 and L_2 peaks, which is a symmetry independent way of determining the filling of the d bands [30]. The L_3/L_2 ratio alone is not a good measure for the oxidation state because the $j-j$ coupling between initial and final states (causing the variation of the L_3/L_2 ratio) is influenced by symmetry changes apparent at grain boundaries. Our analysis indicates a less filled d band at the grain boundary. Comparing this analysis with the results from bulk manganites [77] suggests a 4+ oxidation state of Mn in the bulk and a 3+ oxidation state at the grain boundary core.

To obtain the atomic column resolved ELNES of the $\text{O-}K$ edge, we sacrificed energy resolution for the sake of increased signal. The π^* and σ^* peaks are not resolved in Fig. 16. To clarify whether the observed changes in the ELNES can be correlated to a structural change for examples of the anions, we performed multiple scattering calculations with the same energy resolution as the experiment. For these calculations we used the same structure as for the pristine 36° grain boundary and replaced the Ti in the 2×1 reconstructed columns with Mn . The results in Fig. 17 show an extremely good correlation between experiment and theory. The observed changes of the $\text{O-}K$ edges at the grain boundary therefore primarily reflect the reduced symmetry at the location where the spectra are taken.

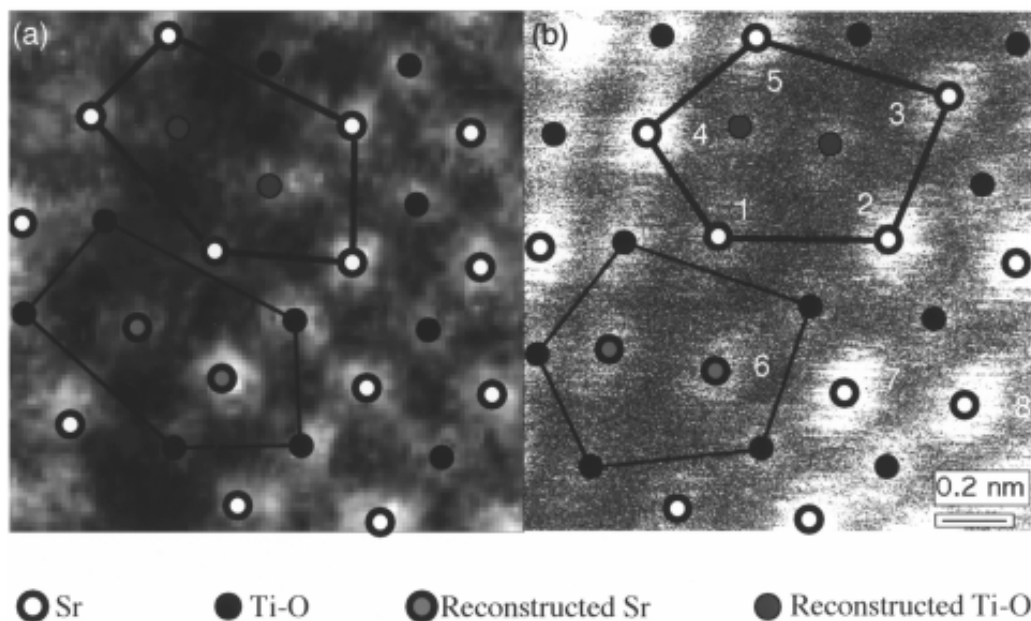


Fig. 14. High magnification Z -contrast image of a nominally undoped $\Sigma 5$ 36° $[001]$ tilt grain boundary in SrTiO_3 (a) and (b) high-magnification Z -contrast image of the $\Sigma 5$ 36° $[001]$ tilt grain boundary after Mn doping.

It should be noted that the spectra described earlier for the pristine boundaries represent an integration over the entire boundary plane and so the column to column fluctuations in fine structure on this scale were not observed.

These results indicate that the cation grain boundary structure can reliably be determined with Z -contrast imaging and that with the $\text{Ti-L}_{2,3}$ edge and the O-K edge data, we can go further and show that octahedral coordination is maintained, although distorted, at *both* doped and pristine grain boundaries. Intrinsically, such studies also give us information that shows the valence state of the Mn acceptors to be +3 in the boundary plane and +4 only 1nm away from the boundary plane (this information is only available by EELS). For the future, to fully understand what is happening at these grain boundaries and determine whether oxygen vacancies play a role in determining the Mn valence and the electrical activity, we need to perform the EELS measurements with higher energy resolution (i.e. resolve the π^* and σ^* peaks). We also need to employ more sophisticated ab-initio simulations to interpret the data. However, that said, the experimental pathway is well defined and we should be able to use this approach to finally be able to reveal the microscopic origin of electrical activity at grain boundaries in perovskites.

3.2. $\text{YBa}_2\text{Cu}_3\text{O}_{7-\delta}$

As one of the first high- T_c superconductors to be discovered [78], the electrical properties of grain boundaries in $\text{YBa}_2\text{Cu}_3\text{O}_{7-\delta}$ (YBCO), have been well docu-

mented over the last ten years [79-81]. Essentially, it has been found that the critical current, J_c , that can be passed across a grain boundary falls off exponentially with increasing misorientation angle [79-81]. There have been several models to account for this that have focussed on the suppression of the superconducting order parameter by the long range strain fields around the dislocation cores in the boundary plane [82,83]. However, at larger angle grain boundaries, the overlap of the individual strain fields [71] may make the use of such concepts inappropriate. As we have shown from the study of grain boundaries in SrTiO_3 (previous section) there is an alternative formalization to consider dislocation cores at grain boundaries; the structural unit model. Here we discuss the structural unit model for high-angle grain boundaries and how it can be used to infer the properties of both low- and high-angle boundaries.

As can be seen from the Z -contrast image of a high-angle $[001]$ tilt grain boundary in YBCO shown in Fig. 18, the grain boundary plane is composed of the same structural units as the SrTiO_3 $[001]$ tilt boundaries (Fig. 12) [84]. Given that the two materials are both perovskites with similar lattice parameters (for YBCO $a \sim b \sim 3.8 \text{ \AA}$ and for SrTiO_3 $a = b = 3.905 \text{ \AA}$) and that this YBCO thin film was grown by laser ablation [85] on a SrTiO_3 bicrystal substrate, this similarity may not be surprising. However, it does mean that we can use similar concepts to understand the properties of YBCO boundaries as were developed for SrTiO_3 in the previous section. One major point that should be noted for the analysis to follow, is that high-resolution TEM

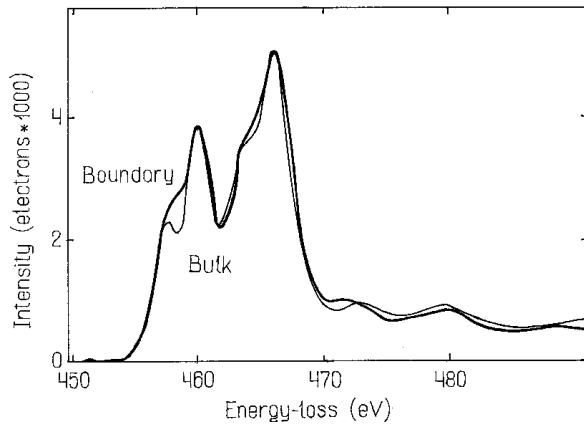


Fig. 15. Ti L -edges from the bulk and the grain boundary plane in the Mn doped sample.

and Z -contrast imaging results from YBCO films grown on various substrates have shown the grain boundary planes to be faceted on the nanometer length scale with a predominantly asymmetric boundary plane [84, 86,87]. For this type of boundary, the Z -contrast images show that the structural units exist with the reconstructed columns on the Cu-O sub-lattice (equivalent to the Ti-O sub-lattice in Fig. 12). Given that the integrity of the Cu-O planes is known to be key to the doping in the bulk structure, the disruption of these planes is already a good indication as to why there is a decrease in the critical current at grain boundaries.

Further information on the effect of these structural units on the doping at the grain boundary plane can be obtained from EELS [88-90]. In particular, for p -type superconducting compounds, such as YBCO, the doping mechanism can be explained by considering the structure to consist of conduction CuO_2 layers separated by charge reservoir blocks. The interaction of the charge reservoir blocks with the conduction layers leads to the formation of the charge carrying holes in the predominantly Oxygen $2p$ -Copper $3d$ valence band. As EELS is sensitive to the density of unoccupied states in the region of the Fermi surface, this means a quantified measurement of the number of charge carriers can in principle be obtained from both oxygen and copper core-edge spectra. For EELS in the STEM, the characteristic core edges that are readily accessible by the spectrometer are the oxygen K -edge ($1s \rightarrow 2p$ transitions) and the copper $L_{2,3}$ -edge ($2p \rightarrow 3d$ transitions). For YBCO, the most accurate means of quantifying the number of holes is through the pre-edge feature on the oxygen K -edge [89] using a series of Gaussian functions (Fig. 19). Using this method, the hole concentration can be quantified to $\sim 5\%$ accuracy. Also shown in Fig. 19 is a quantified measurement of the hole concentration around a 30° $[001]$ tilt asymmetric

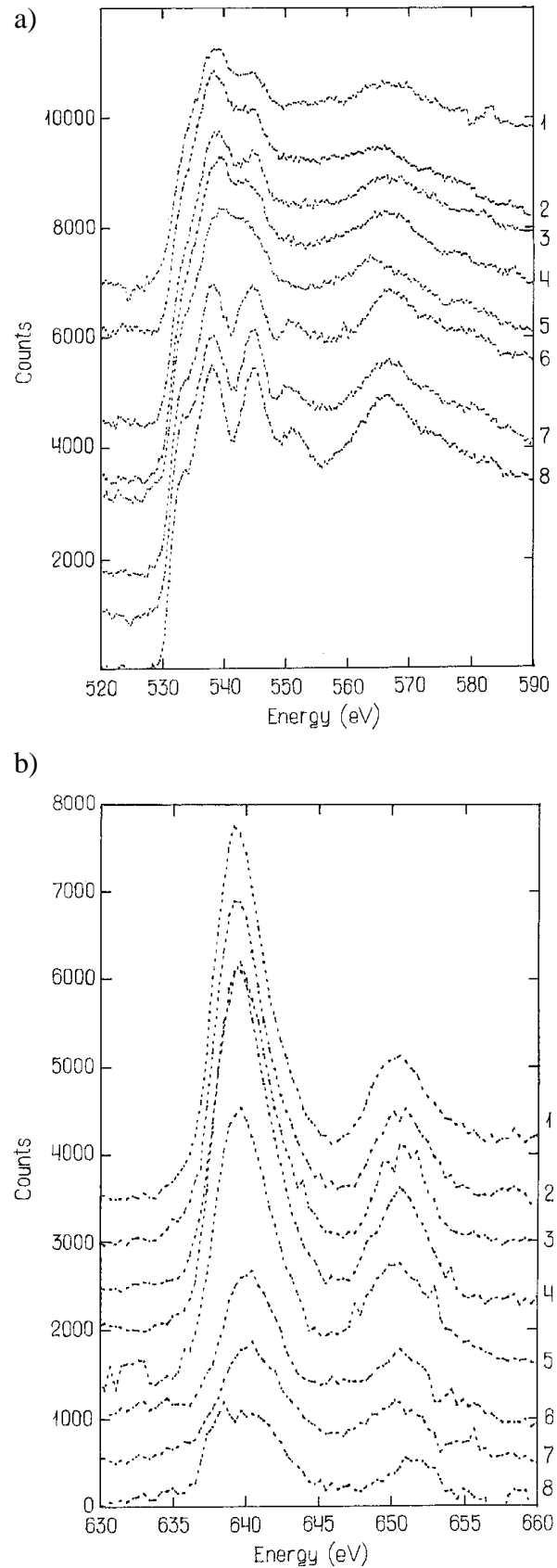


Fig. 16. (a) Oxygen K -edge spectra and (b) manganese L -edge spectra taken from atomic locations defined in the Z -contrast image shown in Fig. 14.

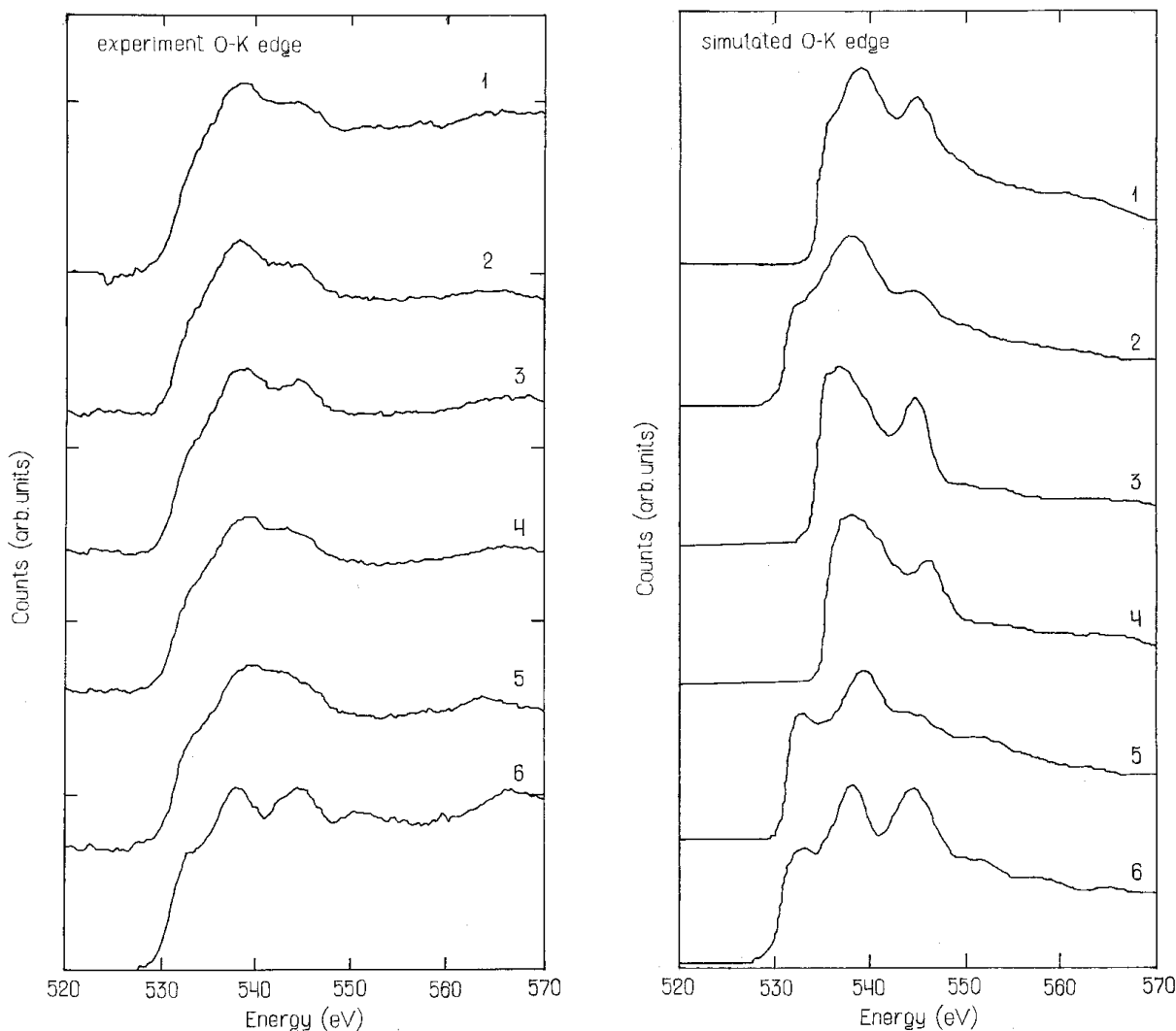


Fig. 17. Comparison between experimental oxygen *K*-edge spectra and multiple scattering simulations of the distinct oxygen sites in the Mn doped grain boundary plane.

grain boundary in a YBCO film grown by laser ablation [91]. As can be clearly seen from the profile, there is a significant depletion in the number of charge carriers at the grain boundary.

To investigate the origin of this charge depletion at grain boundaries, we can use the bond-valence analysis described earlier. In a perfect unit cell of YBCO, the valences of most of the elements involved change very little between YBCO_7 and YBCO_6 (<10%). The exception to this is copper. In fully oxygenated YBCO the copper (1) valence is ~ 2.3 , whereas in fully oxygen deficient YBCO the copper valence is ~ 1.2 [94], although the copper (2) valence changes by <10%. This implies that the copper (1) valence can be used as a very sensitive measure of the number of charge carriers present in the structure. To investigate this effect further, the structures of asymmetric boundaries at other misorientation angles were constructed from the structural units using continuity of grain boundary struc-

ture principles [70]. As a first approximation the boundaries were considered to be straight, i.e. consist of one particular grain boundary plane. For boundary misorientations of 11.4° (boundary plane (100)/(510)), 18.4° (boundary plane (100)/(310)), 26.6° (boundary plane (100)/(210)), 33.7° (boundary plane (100)/(210)), and 45° (boundary plane (100)/(110)), the copper (1) valence as a function of distance from the boundary core can then be calculated from bond-valence sum analysis. In Fig. 20, the valence of each copper (1) site is plotted against its distance from the boundary. Again, it is clear from this plot that the boundary perturbs the local electronic structure sufficiently to create a non-superconducting zone, but more importantly, it is seen that the width of this zone increases with misorientation angle. These plots can now be used to define a grain boundary width.

An alternative approach to defining the grain boundary width, which is equally valid, is to use the

Table 1. The distinct structural units shown in Fig. 12 can be combined to form all [001] tilt grain boundaries in YBCO. Assuming that each structural unit corresponds to an «equivalent» oxygen vacancy allows a density of localized states in the boundary to be determined, and a corresponding depletion layer to be calculated from Eq. 3.

Boundary Plane	Localized States/m ²	Depletion Layer Width, Å
(100) ₁ /(510) ₂	6.9x10 ¹⁷	0.89
(100) ₁ /(410) ₂	8.5x10 ¹⁷	1.11
(100) ₁ /(310) ₂	1.1x10 ¹⁸	1.45
(100) ₁ /(210) ₂	1.6x10 ¹⁸	2.08
(100) ₁ /(320) ₂	2.0x10 ¹⁸	2.61
(100) ₁ /(110) ₂	2.8x10 ¹⁸	3.59

semiconductor picture and consider the formation of a Schottky barrier at the grain boundary [92,93]. This Schottky barrier leads to a charge depletion layer above T_c , and therefore a lack of superconducting charge carriers when the material is cooled below the transition temperature. In this model, we do not consider the details of the grain boundary arrangement as we do with the bond-valence scheme, only we say that each of the structural units is responsible for the formation of a localized electronic state in the grain boundary plane. Using standard dislocation core models for the distribution of each structural unit as a function of the misorientation angle [71], we can therefore calculate the density of localized states that is present for each boundary plane (Table 1).

If we view this excess of charge as a 2-dimensional sheet, we can expect that this results in a compensating depletion layer either side of the boundary, the width of which is given by [1]

$$S_{gb} = N_{bulk} \omega, \quad (3)$$

where S_{gb} is the number of localized boundary states, N_{bulk} is the bulk carrier doping and ω is full width of the depletion zone. As we know the number of localized states at the boundary increases with misorientation angle, it is easy to see the depletion layer width must do the same. To quantify the width of the depletion zone at grain boundaries we need only insert the value of the bulk carrier doping ($N_{bulk} = 4/3V_{cell}$). Using this criterion, the depletion zone width can be calculated. In the same way as for the bond-valence model, we have therefore obtained an increasing barrier width with increasing misorientation angle. Which model contains the most accurate representation of the physical process involved has yet to be determined (the bond-valence model is structural, which must obviously have some validity, but the potentials are empirical and can therefore lead to errors, while the Schottky model does not consider the origin of the charge states).

With either the bond-valence picture or the Schottky barrier model, we have an increasing barrier width with increasing misorientation angle. The magnitude of the superconducting tunneling current across a barrier can be calculated from

$$J_c = J_{c0} \exp(-2k\Delta) \quad (4)$$

where J_{c0} is the bulk critical current, Δ is the interface (depletion layer) width and k is the decay constant (7.7/nm) [94]. For each of the grain boundary misorientations shown in Table 1, the width can be used to determine the expected tunneling current for a constant applied voltage: the criterion used experimentally to measure critical currents. In Fig. 21, the tunneling current as a function of misorientation angle

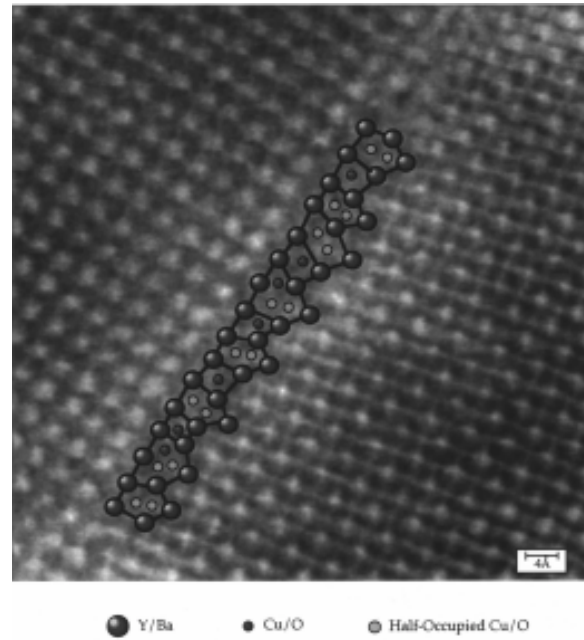


Fig. 18. Z-contrast image of a high-angle [001] tilt boundary in YBCO. The structural units are the same as those observed for SrTiO₃ grain boundaries.

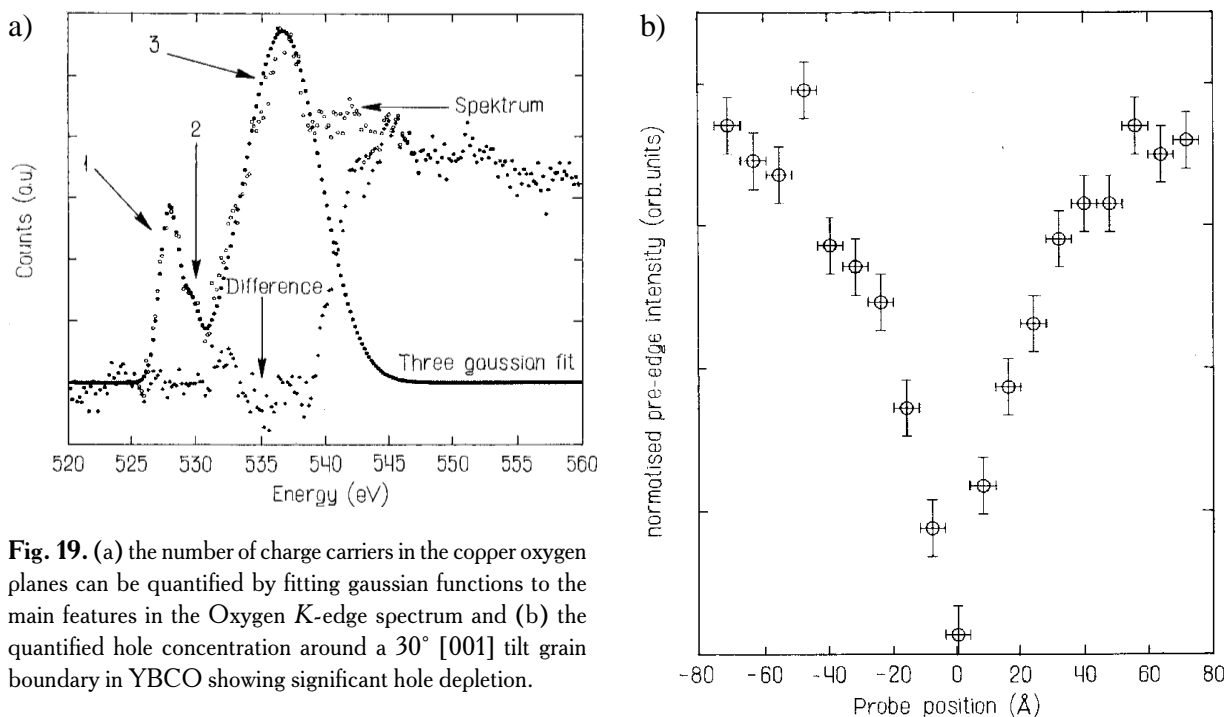


Fig. 19. (a) the number of charge carriers in the copper oxygen planes can be quantified by fitting gaussian functions to the main features in the Oxygen *K*-edge spectrum and (b) the quantified hole concentration around a 30° [001] tilt grain boundary in YBCO showing significant hole depletion.

for asymmetric boundaries is plotted and compared with a range of experimental critical current measurements (here the widths are taken from the Schottky model, but can equally well be taken from the bond-valence model). For the boundary widths defined above, the structural unit model quantitatively reproduces the trend of exponentially decreasing critical current with increasing misorientation angle. The fact that the line goes through the highest values of the experimental data is to be expected as in this analysis we have only considered the intrinsic effect of the boundary. If we add the effect of processing induced oxygen deficiency, the charge depletion width would obviously increase, thereby lowering the critical current. This could be a reason for the scatter in the experimental J_c values. It should also be noted that this analysis can be extended to low-angle grain boundaries. Rather than using the strain field to estimate the relative area of superconducting material, we now use the relative area caused by the distribution of the structural units. As such, the structural unit model can cover the whole range of misorientation angles.

3.3. $\text{Bi}_2\text{Sr}_2\text{Ca}_2\text{Cu}_3\text{O}_{10}$

Another perovskite material that is currently being developed for technological applications is $\text{Bi}_2\text{Sr}_2\text{Ca}_2\text{Cu}_3\text{O}_{10}$. Highly-textured Ag-sheathed $(\text{Bi,Pb})_2\text{Sr}_2\text{Ca}_2\text{Cu}_3\text{O}_{10}$ (Bi-2223) composite tapes have significant potential for the development of superconducting motors, magnets, and transformers. The Bi-2223 phase is one of the Bi-based superconductors (BSCCO) that are represented by the general formula

$\text{Bi}_2\text{Sr}_2\text{Ca}_{n-1}\text{Cu}_n\text{O}_y$ (where $n=1, 2$ or 3). Although relatively high critical-current density (J_c) values up to 70kA/cm^2 have been obtained in multifilamentary Bi-2223/Ag tapes, these J_c values are still less than a few percent of those of thin films [64]. This suggests that even though the cores are textured, grain boundaries still have strong effects on the supercurrent transport phenomena. From a morphological point of view, several models have been proposed to describe the current transport mechanisms in the BSCCO/Ag tapes. However, since the large-scale configuration of the boundaries are mainly considered in these models, the underlying mechanism controlling the properties has yet to be clarified. In order to elucidate the role of the grain boundaries, detailed studies on the atomic structure as well as the chemistry change at the boundary are required.

Here we use the Z-contrast imaging technique to analyze Bi-2223/Ag tapes containing 19 filaments and have a J_c level of more than 60kA/cm^2 at 77K in self field (provided by American Superconductor). Short and transverse cross section samples were prepared by the standard TEM sample preparation methods. The microscopic study was performed in the JEOL 2010F TEM/STEM described in earlier sections. As the lattice parameter for this material is quite large, $\sim 0.4\text{nm}$, the size of the electron probe used for the experiments was selected to be 0.16 nm to increase the signal/noise in the images [18].

The majority of the grain boundaries observed in these tapes are *c*-axis twist boundaries. Fig. 22 shows twist boundaries that are imaged with the incident beam

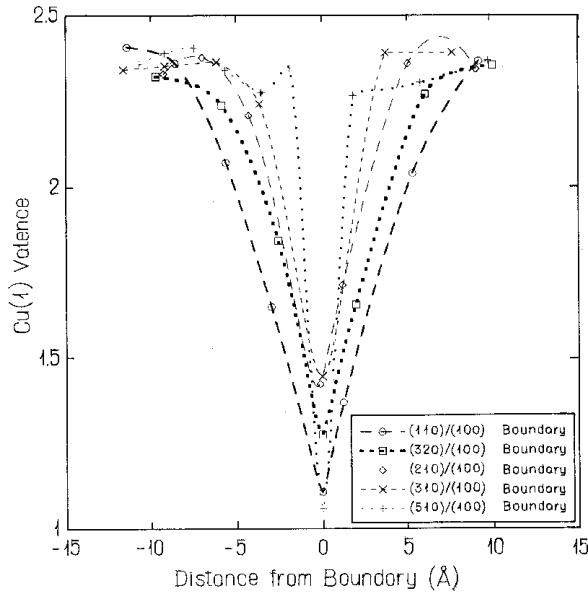


Fig. 20. The Cu(1) valence (calculated from the structural units using bond-valence analysis) as a function of distance from the grain boundary plane for a series of high-angle [001] tilt grain boundaries in YBCO.

oriented parallel to the [110] direction in the upper half of the images. In the lower half several sets of two bright lines are observed which correspond to the BiO double layers viewed end on. From these images it is quite obvious that the boundary is atomically flat and located in the middle of the double BiO layers. Such results are consistent with previous conventional high-resolution TEM images [95], but the advantage of Z-contrast imaging is that the nature and the location of the boundary can be directly identified from the raw images without simulation. Another key point from these images is that although no amorphous layers are observed at the boundaries, local phase variations are often observed (the lack of a phase variation shown in Fig. 22 (a) is actually the minority case). In Fig. 22 (b) three unit cells of Bi-2212 phase are observed on the upper side of the boundary and a half unit cell of Bi-2201 phase on the lower part are present ($T_c=20\text{K}$ as opposed to 110K for Bi-2223). Also, in the lower part of the image a half unit cell of the Bi-2234 phase is seen near the boundary. Both the type and number of phases formed at/near the boundary is found to vary from boundary to boundary. Such local phase variations at/near the boundary should have a strong influence on the local transport phenomena of the supercurrent as the thickness of the secondary phases is typically larger than the coherence length, especially in the framework of the brick-wall model [96].

Another typical set of grain boundaries usually present in BSCCO/Ag tapes is small-angle c -axis tilt boundaries. A characteristic of this type of the bound-

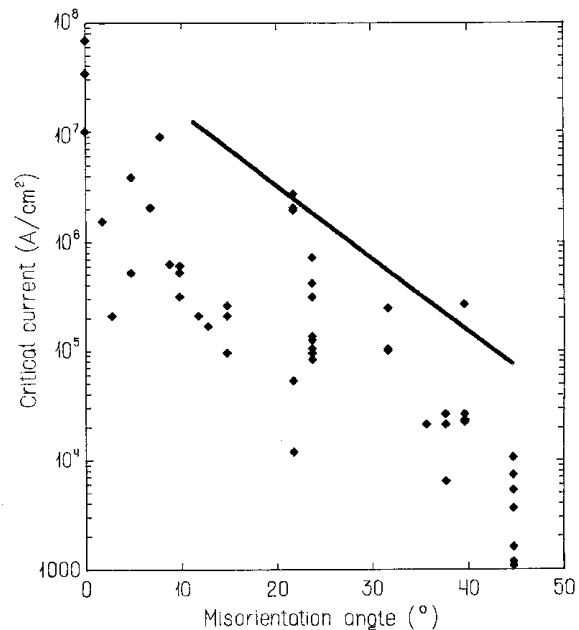


Fig. 21. A comparison of the tunneling current calculated from the grain boundary widths shown in Table 1 with the experimental J_c measurements from a number of research groups.

ary is that basal planes of one grain are parallel to the grain boundary plane. This type of boundary has been considered to play a dominant role in transporting the supercurrent in the railway-switch model [97]. Fig. 23 shows an 11° tilt boundary imaged with the incident beam oriented parallel to [110] orientation of each grain. These two images were obtained from the same area (there is a slight mis-tilt precludes imaging both grains simultaneously). Periodic formation of the $n=1, 2, 3$ and 4 phases in upper grain and $n=2$ and 3 in the lower grain is observed along the boundary. Since the angle between the [110] of both grains is less than 0.1° , a grain boundary structure can be constructed from these two images. Fig. 23 shows a schematic diagram of the grain boundary structure. In this figure, we can see again that the boundary forms on the BiO layers and that the type of phase formed varies periodically along the boundary. We should also note that this periodic formation of different phases at the boundaries is also observed at small-angle c -axis tilt boundaries with a twist component. These different phases are expected to have different transport properties and the periodic local formation of different phases along a grain boundary plane may have important effects on the supercurrent transport not only through c -axis twist boundaries but also through small c -axis tilt boundaries, i.e. weak links are formed.

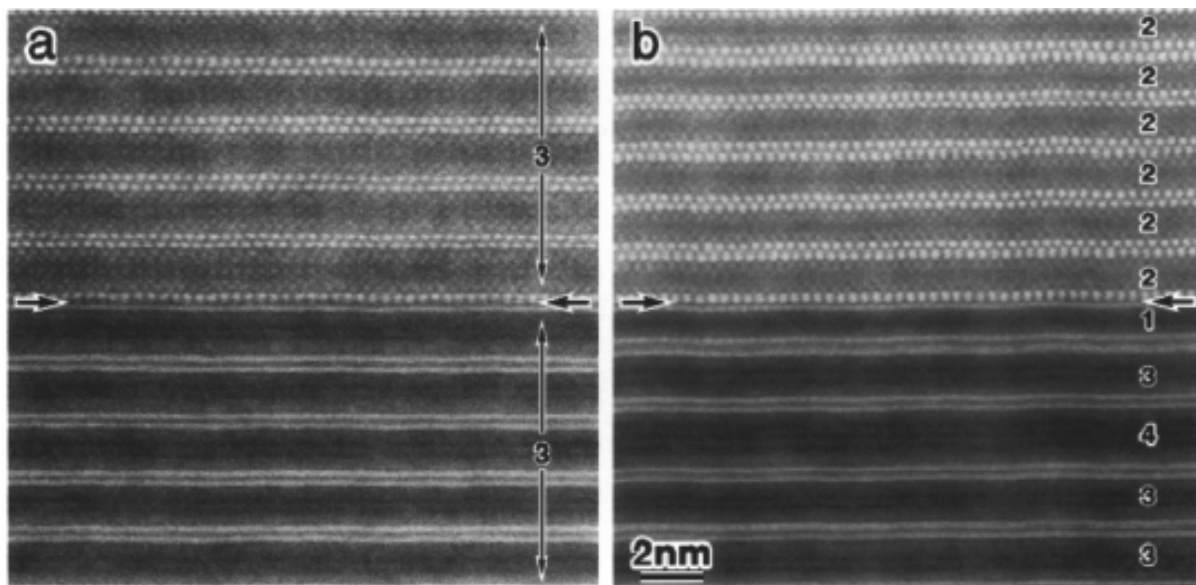


Fig. 22. Z-contrast images of the *c*-axis twist boundaries in Bi-2223/Ag tapes (a) without and (b) with local phase variations at/near the boundary. Positions of the grain boundaries are indicated by arrows. The numbers (*n*) in the figures represent the types of phases ($\text{Bi}_2\text{Sr}_2\text{Ca}_{n-1}\text{Cu}_n\text{O}_y$).

4. HETEROPHASE INTERFACES

The examples that we have considered so far have concerned the determination of the structure and bonding at homo-phase interfaces, i.e. those interfaces where the material either side of the interface is the same. We now turn our attention to hetero-interfaces where the material on either side of the interface is different. This is the type of interface that is prevalent in semiconductor devices where the interface is either between the substrate and a thin film or between the different electronic components in the device, e.g. metal-oxide, semiconductor-oxide, metal-semiconductor.

4.1. GaAs/Au

The first example [98] that we will consider here is the interface between gallium arsenide (GaAs) and Gold (Au). This particular system has been studied extensively in an effort to ascertain the fundamental physics behind the formation of Schottky or Ohmic contacts between metals and semiconductors. An ohmic contact between GaAs and Au was fabricated by alloying at 420° C for 15 seconds after growth. The interface region exhibits spiking with Au protruding approximately 50 nm into the GaAs. The Au grains are aligned with the (1 $\bar{1}$ 0) plane approximately parallel to the interface. Fig. 24 shows a Z-contrast image at relatively low magnification showing one of the Au spikes, and the atomic resolution structure of the interface 50 nm away from the spike is shown in Fig. 25. The image shows Au terminating on the (1 $\bar{1}$ 0) plane which results in a lattice mismatch of 2.5% with respect to the (001) terminated

GaAs. An atomic step in the interface is present near the image center and the resolution here is approximately 0.15 nm. In Fig. 26 an angled section of one of the protruding spikes is shown. The Au forms a (111) tilt boundary with GaAs (the angle is approximately 18°) and a twin boundary is seen in the bulk Au where the angle of the interface changes. Finally, Fig. 26 also shows a third example of the interface structure along one side of a spike. Au is faceted along the close packed {111} plane with steps every one to two atomic columns. These preliminary results show that it is possible to identify the interface structure in heterophase interfaces directly using the Z-contrast technique. Work is continuing in this area to correlate the types of interface structures with the electronic properties. This will be achieved by a comparison with Schottky interfaces and also by looking at the Ni/GaAs system where EELS can be used to investigate the bonding changes at the interface.

4.2. CdTe / Si (As)

As a final example of the use of STEM to investigate interface properties, we show an analysis of the effect of Arsenic (As) passivation of Silicon (Si) substrates on the subsequent growth of the II-VI semiconductor Cadmium Telluride (CdTe) [99, 100]. The interest in the growth of CdTe on Si is motivated by its potential use as an alternative substrate for the subsequent growth and fabrication of $\text{Hg}_{1-x}\text{Cd}_x\text{Te}$ infrared detectors [101,102]. In this regard, the growth of single domain CdTe with the (111)B orientation (a short notation for the Te polar surface, with (111)A denoting the Cd po-

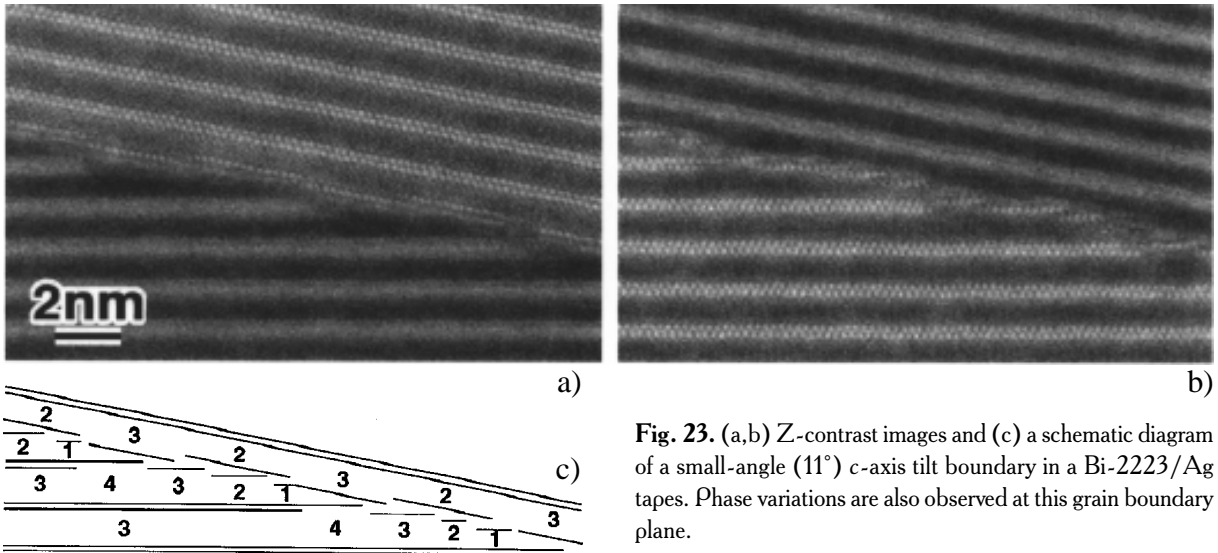


Fig. 23. (a,b) Z-contrast images and (c) a schematic diagram of a small-angle (11°) *c*-axis tilt boundary in a Bi-2223/Ag tapes. Phase variations are also observed at this grain boundary plane.

lar (111) surface), is particularly desirable as this orientation requires the least Hg flux for growth of $\text{Hg}_{1-x}\text{Cd}_x\text{Te}$ by molecular beam epitaxy (MBE) [103]. This is also the standard orientation for HgCdTe growth in liquid phase epitaxy, and could be used for CdS/CdTe high efficiency solar cells grown by MBE.

In this work, two films were grown by MBE on nominal Si (111) substrates under similar growth conditions except that the substrates were cooled under a different initial flux, i.e. either As flux or Te flux. The microstructures of the two films grown on the Te and As treated Si (111) substrates are shown in Fig. 27. It is immediately obvious from the low magnification images that the two films have different structural features. The film grown on the Te treated substrate has very faulted microstructure, containing different

twin grains, planar defects on two sets of {111} planes, and threading dislocations (Fig. 27(a)). Furthermore, the polarity of the film is determined to be (111)A from the convergent beam electron diffraction (CBED) pattern (Fig. 27(b)). The film-substrate interface is also very rough, with 15nm modulations into the Si substrate due to the Te flux reacting with Si during cooling (Fig. 27(c)). A very different quality of film is observed for growth on the As-passivated substrate (Fig. 27(d)). Apart from the few wide lamellar microtwins confined to the $0.8\ \mu\text{m}$ region close to the interface and a few threading dislocations, the epilayer is single crystal with excellent structural quality over large areas. Double crystal X-ray rocking curves from the CdTe (333) reflection using $\text{Cu-K}\alpha_1$ and a Si (133) crystal

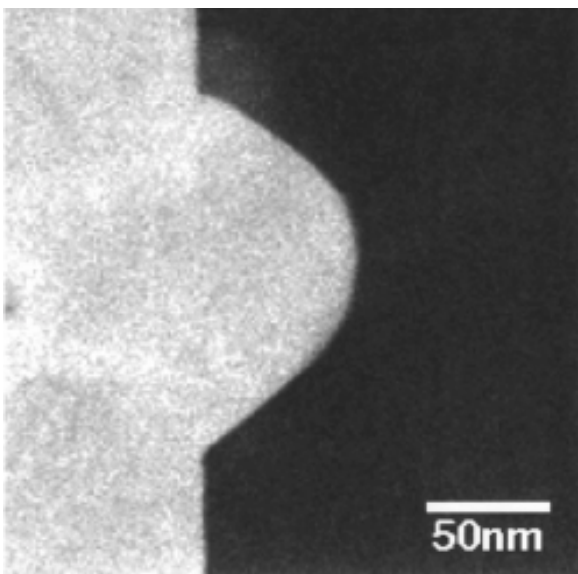


Fig. 24. Low-magnification Z-contrast image of the Au spikes protruding into GaAs at the GaAs/Au interface.

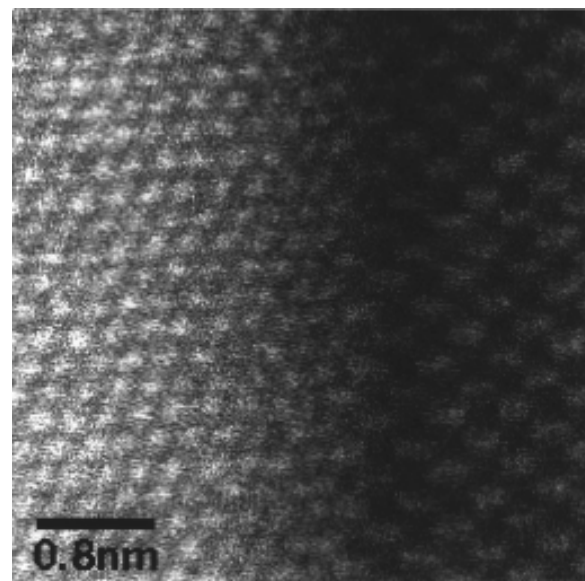


Fig. 25. Atomic resolution image of the interface ~ 50 nm away from the Au spike.

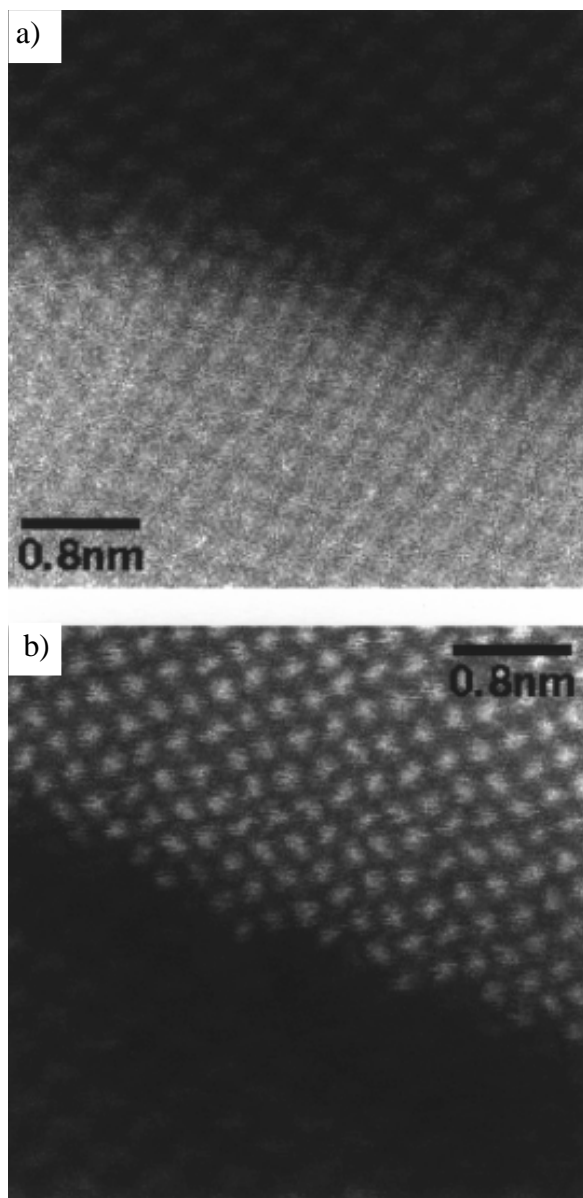


Fig. 26. (a) and (b) Atomic resolution Z -contrast images of the interface structure in the Au spike.

monochromator gives measurement of the full width at half maximum (FWHM) of 87 arcseconds for a 5 μm thick layer. The selected area diffraction pattern from the CdTe/Si interface shows the perfect alignment of CdTe (111) layer relative to the Si (111) substrate (Fig. 27(e)). The polarity of the film is confirmed to be (111)B by CBED (Fig. 27(f)). We should note at this point that this initial analysis of the general film microstructures highlights one of the advantages of the modern TEM/STEM instruments, i.e. that you can perform detailed phase contrast imaging and diffraction work in TEM mode prior to the more detailed STEM analysis.

The difference in the quality of the films therefore appears to be related to the difference in the initial flux treatment of the Si (111) surface. Examining the CdTe/

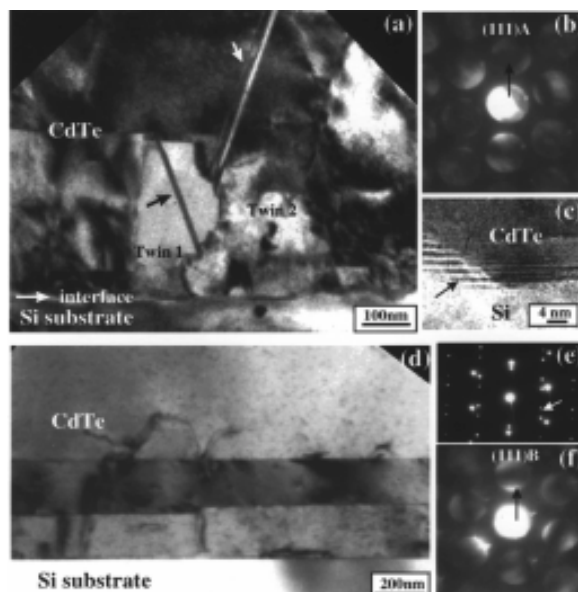


Fig. 27. (a) Low magnification bright field TEM image showing a cross-sectional view (in the $[1-10]$ direction) of the sample grown on Te treated Si(111) substrate. The image highlights the presence of many twin domains, planar defects and threading dislocations and the inset CBED pattern shows the film has the (111) A polarity. (b) Low magnification bright field TEM image showing a cross-sectional view (in the $[1-10]$ direction) of the sample grown on the As passivated Si (111) substrate. The image shows a very large area of high crystalline quality with only the presence of lamellae twins being observed close to the interface with the substrate. The inset selected area diffraction pattern shows the alignment of the epilayer with the substrate and the inset CBED pattern shows the film has the (111) B polarity.

Si interface by energy dispersive X-ray spectroscopy (EDS) shows that the As that is initially deposited on the Si surface remains there for the subsequent growth of the CdTe film (Fig. 28). The three spectra show that only when the 1 nm probe is placed at the interface is there an As signal present (the two other spectra are obtained ~ 5 nm from the interface). Furthermore, quantifying the spectra shown in Fig. 8 gives an estimate of the As concentration close to one monolayer. These results are consistent with the *in situ* reflection high energy electron diffraction (RHEED) observations before initiation of the CdTe growth, and confirmed by x-ray photoemission spectroscopy [104].

Having generated a general picture of the film morphology and the composition of the film-substrate interface we can now move on to examine the interface in more detail using atomic resolution Z -contrast imaging. Fig. 29 shows a raw atomic resolution Z -contrast image of the CdTe/Si interface, and the same image after Fourier filtering. The elongated white spots in the image are atomic columns separated by distances

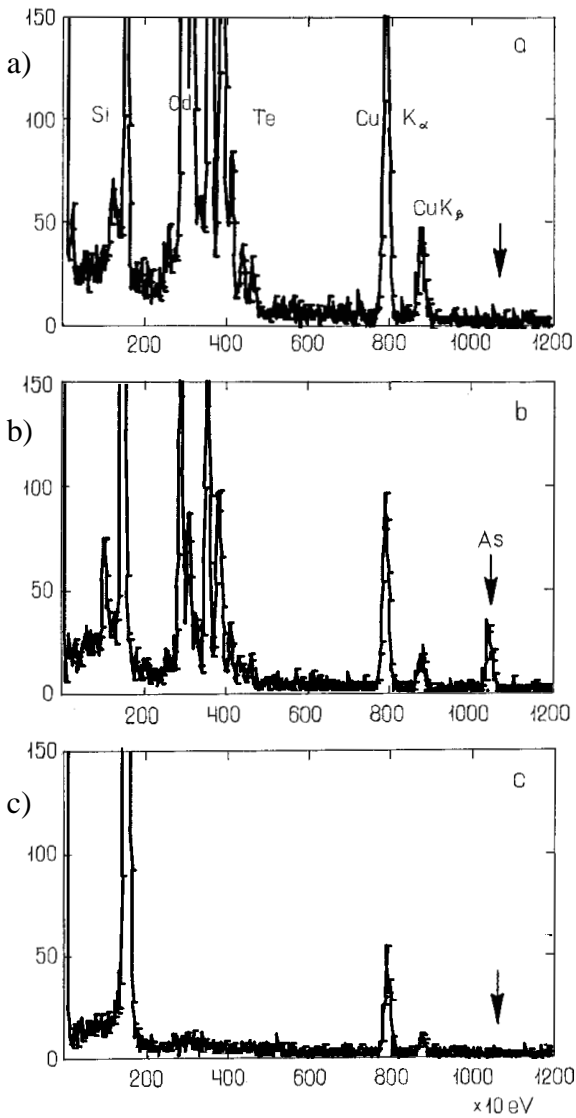


Fig. 28. Energy dispersive x-ray spectra of (a) CdTe layer; (b) CdTe/Si interface; (c) Si substrate, confirming the presence of a monolayer of As at the interface.

smaller than the 1.5\AA resolution of the microscope. The first CdTe layer can be easily ascertained by the intensity difference at the interface, as CdTe has a higher atomic number than Si or As. The extra planes of the misfit dislocations are indicated, and the cores of the misfit dislocations are clearly seen located at the interface between the CdTe film and the substrate. By drawing a Burgers circuit around the cores, the edge component of the Burgers vector is $1/4[112]$, which is parallel to the interface, providing the explanation as to why there is no tilt of the epilayer with respect to the substrate. The average spacing between misfit dislocations is 1.9 nm. These are the grown-in misfit dislocations that have relieved the majority of the mismatch strain.

Z-contrast images (Fig. 29) from a different area along the same interface, show that the first few layers of CdTe can also be deposited in a twinning position relative to the substrate. This indicates that CdTe can initially nucleate in two orientations with a twinning relationship. This means the film adopts either the substrate orientation with ABCABC||ABC ..., or in a twinning position to the substrate with ABCABC||BACBAC ..., where A, B, or C denotes the atomic double layer. It must be pointed out from the high-resolution observations that no islands or grains other than the few coherent twin boundaries are found in the region at the interface, the twinned islands are of small quantity, and the film/substrate interface is atomically flat.

The above experimental observations show that As is crucial in obtaining the desired (111)B film with high crystalline quality. There are two main factors that result in the single domain high crystalline quality epitaxial CdTe (111)B growth on Si(111); the As-

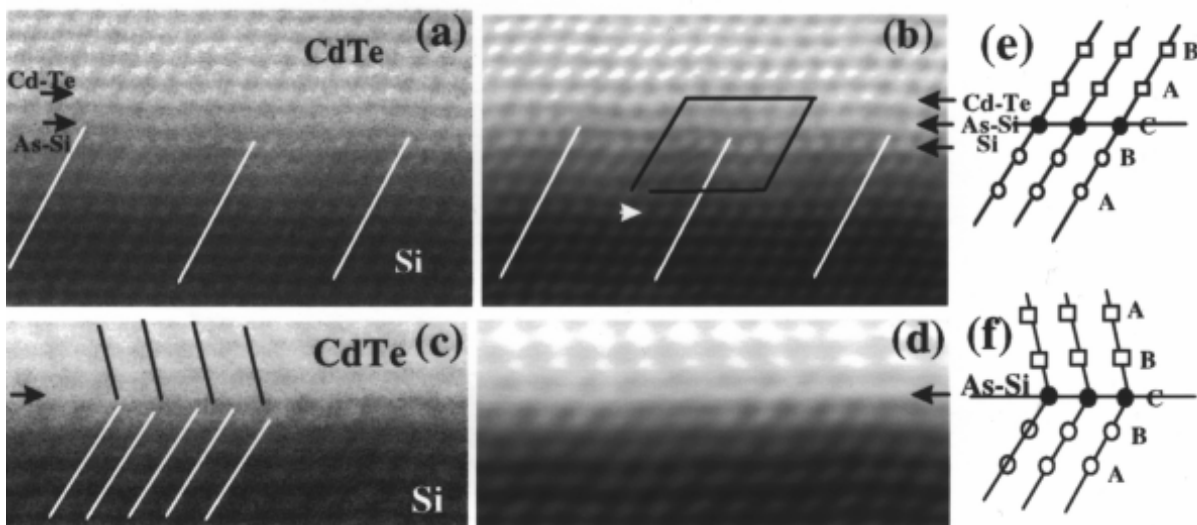


Fig. 29. (a) A raw atomic resolution Z-contrast image of the CdTe/Si interface viewed along the $[1-10]$ direction with (b) showing the Fourier filtered image of (a). (c) Atomic resolution Z-contrast image of a different region along the interface showing twin oriented layer growth with (d) showing the corresponding Fourier filtered image of (c). (e) Schematic showing the two possible orientations of the epilayer corresponding to (a) and (c) respectively (A,B and C denote a double atomic layer).

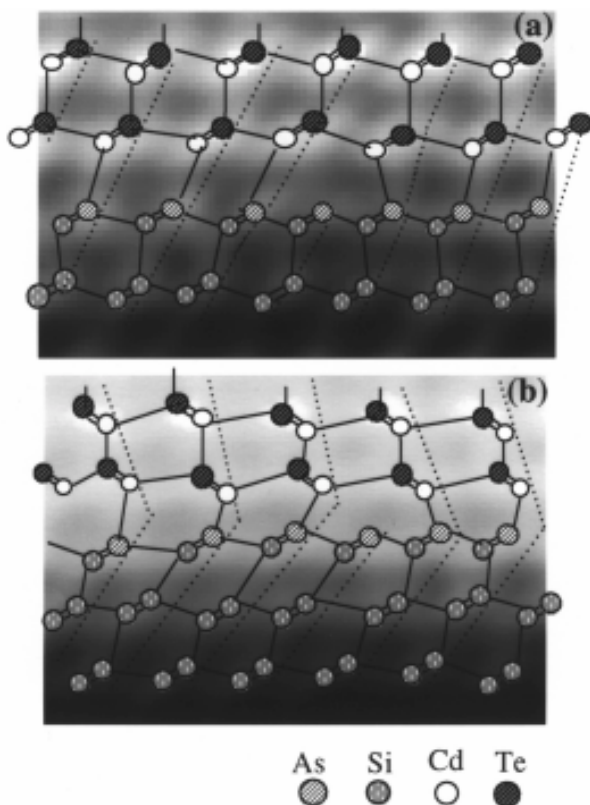


Fig. 30. (a) Sketch of the atomic configuration across the interface of the CdTe(111)B on As passivated Si(111) with a misfit dislocation core superimposed on the experimental Z-contrast image. Cd is the first atomic layer to bond with As, and the structure proceeds from this initiation process into a film with B polarity.

passivated Si(111) surface which results in the (111) B polarity and the nature of atomic steps and terraces on the nominally Si(111) surface which give rise to layer growth free of multi-domains [99]. It is well known that As replaces the outermost Si atoms of the double layer during passivation of the Si(111) surface in the MBE growth process [105], and it is known from the above investigations that As stays there after the growth. Both imply that As is present at the interface as a monolayer separating CdTe and Si during the growth. Based on the As-Cd, As-Te bond formation energies [106], it is likely that Cd is favored as the first atomic layer forming bond with the As at the interface, where the bonding configuration proceeds in a fashion such as Si-As-Cd-Te across the interface as shown in Fig. 30.

Even though it is known that Cd atoms have a very low sticking coefficient and would re-evaporate from the surface under only a Cd flux, the resultant CdTe (111) B layer growth implies that the presence of Te atoms supplied by stoichiometric flux is sufficient to stabilize the Cd on the surface. This occurs through a transition layer at the growth front. CdTe is initiated with Cd atoms forming one bond with As and three

bonds with Te, producing a Te stabilized growth surface, which finally results in the (111) B growth. Because of the high interfacial energy associated with the large lattice mismatch between CdTe and Si and the requirement of low temperature initiation, layer deposition starts with island nucleation. CdTe nucleation could initiate both at step edges and on the terraces, and because the atomic structures of the Si (111) surface comprise double layer steps giving the same atomic configuration from terrace to terrace, all the nuclei would have only two possible positions, i.e. the twinning positions. In this system, the associated lattice mismatch energy is the same for the two possible depositions. However, the twinning position nuclei might have a higher interfacial energy due to the “faulted” stacking sequence across the interface, and therefore the majority of the nuclei would adopt the orientation of the substrate (as is observed experimentally). Growth then proceeds in layer by layer fashion soon when the substrate temperature is raised to normal growth temperature after several tens of monolayer deposition. Because there is no tilt between the nucleating islands, the coherent double positioning boundaries are easily eliminated after a short nucleation stage.

5. CONCLUSIONS

The ability to perform detailed atomic scale analyses of interfaces using correlated Z-contrast imaging and EELS is now well established on commercially available microscopes. The further addition of other techniques, such as EDS, CBED and phase contrast imaging, will further enhance the level of characterization possible in the future. Such information allows us to begin to unravel the complexities of the structure, composition and bonding changes that can occur at interfaces and from that, develop a fundamental understanding of the structure-property relationships. For many materials systems currently being developed, this can provide the pathway to the realization of new technologies.

ACKNOWLEDGMENTS

Aspects of this work were performed in collaboration with S. Sivanathan, S. Rujiwarat, P. D. Nellist, V. P. David, K. D. Johnson, R. P. Rodrigues, F. Omnés, B. Beaumont, J. P. Faurie, P. Gibart, J. L. Reno and A. G. Baca. The microscope facilities at UIC were purchased with support from the NSF under grant number DMR-9601792. Research performed on the semiconductor systems was supported by NSF under grant number DMR-9733895, research on the superconductors was supported by NSF under grant number DMR-9803021,

and research on SrTiO₃ was supported by DOE under grant number DE-FG02-996ER45610. This research was also supported in part by contract number DE-AC05-96OR22464 with Lockheed Martin Energy Systems.

REFERENCES

- [1] A. P. Sutton and R. W. Balluffi, *Interfaces in Crystalline Materials* (Oxford University Press, 1995).
- [2] See for example, *Materials Interfaces*, ed. by D. Wolf and S. Yip (Chapman & Hall, 1992).
- [3] D. A. Muller, D. A. Sashkov, R. Benedek, L. H. Yang, J. Silcox and D. N. Seidman // *Phys. Rev. Letts.* **80** (1998) 4741.
- [4] A. Zalar, B. M. M. Baretzky, S. Hofmann, M. Ruhle and P. Panjan // *Thin Solid Films* **352** (1999) 151.
- [5] R. Benedek, D. N. Seidman and L. H. Yang // *Microscopy and Microanalysis* **3** (1997) 333.
- [6] D. A. Muller, T. Sorsch, S. Moccio, F. H. Baumann, K. Evans-Lutterodt and G. Timp // *Nature* **399** (1999) 758.
- [7] G. Duscher, S. J. Pennycook, N. D. Browning, R. Rupangudi, C. Takoudis, H. J. Gao and R. Singh, In: *proceedings of Characterization and Metrology for ULSI Technology: 1998 International Conference*, ed. by D. G. Seiler, A. C. Deibold, W. M. Bullis, T. J. Shaffner, R. McDonald and E. J. Walters (American Institute of Physics, 1998)
- [8] D. A. Muller, Y. Tzou, R. Raj and J. Silcox // *Nature* **366** (1993) 725.
- [9] H. Hasegawa, Y. Koyama and T. Hashizume // *Japanese Journal of Applied Physics* **1** **38** (1999) 2634.
- [10] F. Ernst, O. Keinzle and M. Ruhle // *J. Eur. Ceram. Soc.* **19** (1998) 665.
- [11] M. F. Chisholm, A. Maiti, S. J. Pennycook and S. T. Pantelides // *Phys. Rev. Letts.* **81** (1998) 132.
- [12] D. A. Muller // *Phys. Rev. B* **58** (1998) 5989.
- [13] K. L. Merkle and D. J. Smith // *Phys. Rev. Lett.* **59** (1987) 2887.
- [14] M. M. McGibbon, N. D. Browning, M. F. Chisholm, A. J. McGibbon, S. J. Pennycook, V. Ravikumar and V. P. Dravid // *Science* **266** (1994) 102.
- [15] S. J. Pennycook and L. A. Boatner // *Nature* **336** (1988) 565.
- [16] N. D. Browning, M. F. Chisholm and S. J. Pennycook // *Nature* **366** (1993) 143.
- [17] P. D. Nellist and S. J. Pennycook // *Ultramicroscopy* **78** (1999) 111.
- [18] E. M. James and N. D. Browning // *Ultramicroscopy* **78** (1999) 125.
- [19] E. M. James, N. D. Browning, A. W. Nicholls, M. Kawasaki, Y. Xin, S. Stemmer // *J. Electron. Microscopy* **47** (1998) 561.
- [20] J. M. Cowley // *J. Elect. Microsc. Technique* **3** (1986) 25.
- [21] J. M. Cowley // *Appl. Phys. Lett.* **15** (1969) 58.
- [22] P. D. Nellist, B. C. McCallum and J. M. Rodenburg // *Nature* **374** (1995) 630.
- [23] O. L. Krivanek, N. Dellby and A. R. Lupini // *Ultramicroscopy* **78** (1999) 1.
- [24] J. A. Lin and J. M. Cowley // *Ultramicroscopy* **19** (1986) 31.
- [25] D. E. Jesson and S. J. Pennycook // *Proc. R. Soc. (London) A* **441** (1993) 261.
- [26] D. E. Jesson and S. J. Pennycook // *Proc. R. Soc. (London) A* **449** (1995) 273.
- [27] J. Fertig and H. Rose // *Optik* **59** (1981) 407.
- [28] P. E. Batson // *Nature* **366** (1993) 727.
- [29] G. Duscher, N. D. Browning and S. J. Pennycook // *Physica Status Solidi* **166** (1998) 327.
- [30] R. F. Egerton, *Electron Energy Loss Spectroscopy in the Electron Microscope* (Plenum, 1996).
- [31] V. W. Maslen and C. J. Rossouw // *Phil. Mag. A* **47** (1983) 119.
- [32] L. J. Allen and C. J. Rossouw // *Phys. Rev. B* **42** (1990) 11644.
- [33] O. F. Holbrook and D. M. Bird // *Proc. Microscopy and Microanalysis* 1995, **278** (1995).
- [34] S. J. Pennycook, D. E. Jesson and N. D. Browning // *Phys. Rev. B* **96** (1995) 575.
- [35] B. Rafferty and S. J. Pennycook // *Ultramicroscopy* **78** (1999) 141.
- [36] D. Sing, *Plane Waves, Pseudopotentials and the LAPW method* (Kluwer Academic 1994).
- [37] L. Pauling, *The Nature of the Chemical Bond* (Cornell, 1960).
- [38] N. D. Browning, J. P. Buban, H. O. Moltaji and G. Duscher // *J. American Ceramic Society* **82** (1999) 366.
- [39] D. Altermatt and I. D. Brown // *Acta Cryst. B* **41** (1985) 240.
- [40] I. D. Brown and D. Altermatt // *Acta Cryst. B* **41** (1985) 244.
- [41] P. J. Durham, J. B. Pendry and C. H. Hodges // *Computer Phys. Comm.* **25** (1982) 193.
- [42] J. J. Rehr, S. I. Zabinsky and R. C. Albers // *Phys. Rev. Lett.* **69** (1992) 3397.
- [43] A. L. Ankudinov, B. Ravel, J. J. Rehr and S. D. Conradson // *Phys. Rev. B* **58** (1998) 7565.

- [44] R. Brydson, H. Sauer and W. Engle, In: *Transmission Electron Energy Loss Spectrometry in Materials Science*, ed. by M.M. Disko, C.C. Ahn and B. Fultz (The Minerals, Metals and Materials Society, Warrendale, PA, 1992) p 131.
- [45] N. D. Browning, H. O. Moltaji and J. P. Buban // *Phys. Rev. B* **58** (1998) 8289.
- [46] D. C. Koningsberger, In: *X-ray absorption: Principles, Applications, Techniques of EXAFS, SEXAFS and XANES*, ed. by D. C Koningsberger and R. Prins (Wiley, N.Y., 1987).
- [47] Y. Xin, E. M. James, I. Arslan, S. Sivananthan, N. D. Browning, S. J. Pennycook, F. Omnes, B. Beaumont, J-P. Faurie and P. Gibart, submitted *Applied Physics Letters*.
- [48] S. D. Lester, F.A. Ponce, M. G. Craford and D. A. Steigerwald // *Appl. Phys. Lett.* **66** (1995) 1249.
- [49] J. Elsner, R. Jones, P. K. Sitch, V. D. Porezag, M. Elstner, T. Frauenheim, M. I. Heggie, S. Oberg, P. R. Briddon // *Phys. Rev. Lett.* **79** (1997) 3672.
- [50] S. Nakamura, M. Senoh, S. Nagahama, N. Iwasa, T. Yamada, T. Matsushita, H. Kiyoku, Y. Sugimoto, T. Kozaki, H. Umemoto, M. Sano and K. Chocho // *Appl. Phys. Lett.* **72** (1998) 211.
- [51] O. Nam, M. D. Bremser and R. F. Davis // *Appl. Phys. Lett.* **71** (1997) 2638.
- [52] S. J. Rosner, E. C. Carr, M. J. Ludowise, G. Girolami and H. I. Erikson // *Appl. Phys. Lett.* **70** (1997) 420.
- [53] T. Sugahara, H. Sato, M.S.Hao, Y. Naoi, S. Kurai, S. Tottori, K. Yamashita, K. Nishino, L.T. Romano and S. Sakai // *Jpn. J. Appl. Phys. part 2* **37** (1998) L398.
- [54] A.F. Wright and U. Grossner // *Appl. Phys. Lett.* **73** (1998) 2751.
- [55] J. Elsner, R. Jones, M. I. Heggie, P. K. Sitch, M. Haugk, V. D. Porezag, Th. Frauenheim, S. Oberg and P. R. Briddon // *Phys. Rev. B* **58** (1998) 12571.
- [56] N.G. Weimann, L.F. Eastman, D. Doppalapudi, H.M. Ng and T.D. Moustakas // *J. Appl. Phys.* **83** (1998) 3656.
- [57] P. J. Hansen, Y. E. Strausser, A. N. Erickson, E. J. Tarsa, P. Kozodoy, E. G. Brazel, J. P. Ibbetson, U. Mishra, V. Narayanamurti, S. P. Den Baars and J. S. Speck // *Appl. Phys. Lett.* **72** (1998) 2247.
- [58] C. Youtsey, L.T. Romano and I. Adesida // *Appl. Phys. Lett.* **73** (1998) 797.
- [59] D. C. Look and J. R. Sizelove // *Phys. Rev. Lett.* **82** (1999) 1237.
- [60] Y. Xin, S. J. Pennycook, N. D. Browning, P. D. Nellist, S. Sivananthan, J. P. Faurie and P. Gibart // *Applied Physics Lett.* **72** (1998) 2680.
- [61] N. D. Browning, J. Yuan and L. M. Brown // *Phil. Mag.* **A67** (1993) 261.
- [62] K. Lawniczak-Jablonska, T. Suski, Z. Liliental-Weber, E.M. Gullikson, J.H. Underwood, R.C.C. Perera and T. J. Drummond // *Appl. Phys. Lett.* **70** (1997) 2711.
- [63] Z. L. Wang and Z. C. Kang, *Functional and Smart Materials* (Plenum, 1998).
- [64]. Q. Li, G. N. Riley, R. D. Parella, S. Fleshler, M. W. Rupich, W. L. Carter, J. O. Willis, J. Y. Coulter, J. F. Bingert, J. A. Parrell and D. C. Larbelestier // *IEEE Trans. Appl. Supercond.* **7** (1997) 2026.
- [65] see for example, *Ferroelectric Thin Films II*, ed. A. I. Kingon, E. R. Myers and B. Tuttle, MRS Symposium Proceedings 243 (1991).
- [66] R. A. McKee, F. J. Walker and M. F. Chisholm // *Phys. Rev. Lett.* **81** (1998) 3014.
- [67] A. Maignan, C. Simon and V. Caignaert // *J. Applied Physics* **79** (1996) 7891.
- [68] N. D. Browning and S. J. Pennycook // *J. Phys. D* **29** (1996) 1779.
- [69] M. M. McGibbon, N. D. Browning, A. J. McGibbon, M. F. Chisholm and S. J. Pennycook // *Phil. Mag. A* **73** (1996) 625.
- [70] A. P. Sutton // *Acta Metall.* **36** (1988) 1291.
- [71] J. P. Hirth and J. Lothe, *Theory of Dislocations* (John Wiley & Sons, N.Y., 1982).
- [72] R. D. Leapman, L. A. Grunes and P. L. Fejes // *Phys. Rev. B* **26** (1982) 614.
- [73] F. M. F. de Groot, J. C. Fuggle, B. T. Thole and G. A. Sawatzky // *Phys. Rev. B* **41** (1990) 928.
- [74] Y.-M. Chiang, D. P. Birnie and W. D. Kingery., *Electro Ceramics* (John Wiley & Sons, N.Y. 1997).
- [75] N.-H. Chan, R.K. Sharma and D. M. Smyth. // *J. Electrochem. Soc.* **128** (1981) 1762.
- [76] N. D. Browning, J. P. Buban, H. O. Moltaji, G. Duscher, S. J. Pennycook, R. P. Rodrigues, K. Johnson and V. P. Dravid // *Appl. Phys. Lett.* **74** (1999) 2638.
- [77] H. Kurata and C. Colliex // *Phys. Rev. B* **48** (1993) 2102.
- [78] M. K. Wu, R. J. Ashburn, C. J. Torng, D. H. Hor, R. L. Meng, L. Gan, Z. J. Huang, Y. Q. Wang and C. W. Chu // *Phys. Rev. Lett.* **58** (1987) 908.
- [79] D. Dimos, P. Chaudhari and J. Mannhart // *Phys. Rev. B* **41** (1990) 4038.

- [80] R. Gross and B. Mayer // *Physica C* **180** (1991) 235.
- [81] Z. G. Ivanov, P. A. Nilsson, D. Winkler, T. Claeson, E. A. Stepanov and A. Ya. Tzalenchuk // *Appl. Phys. Lett.* **59** (1991) 3030.
- [82] M. F. Chisholm and S. J. Pennycook // *Nature* **351** (1991) 47.
- [83] A. Gurevich and E. A. Pashitskii // *Phys. Rev. B* **57** (1998) 13878.
- [84] N. D. Browning, J. P. Buban, P. D. Nellist, D. P. Norton and S. J. Pennycook // *Physica C* **294** (1998) 183.
- [85] D. P. Norton, D. H. Lowndes, J. D. Budai, D. K. Christen, E. C. Jones, K. W. Lay and J. E. Tkaczyc // *J. Appl. Phys.* **68** (1990) 223.
- [86] B. Kabius, J. W. Seo, T. Amrein, U. Dahne, A. Scholen, M. Siegel, K. Urban and C. Schultz // *Physica C* **231** (1994) 123.
- [87] A. F. Marshall and C. B. Eom // *Physica C* **207** (1993) 239.
- [88] N. Nucker, H. Romberg, X. X. Xi, J. Fink, B. Gegenheimer and Z. X. Zhao // *Phys Rev B* **39** (1989) 6619.
- [89] N. D. Browning, J. Yuan and L. M. Brown // *Supercond. Sci. Technol.* **4** (1991) S346.
- [90] N. D. Browning, J. Yuan and L. M. Brown // *Physica C* **202** (1992) 12.
- [91] N. D. Browning, M. F. Chisholm, D. P. Norton, D. H. Lowndes and S. J. Pennycook // *Physica C* **212** (1993) 185.
- [92] H. Hilgenkamp and J. Mannhart // *Appl. Phys. A Mater. Sci. Process.* **64** (1997) 553.
- [93] H. Hilgenkamp and J. Mannhart // *Appl. Phys. Lett.* **73** (1998) 265.
- [94] J. Halbritter // *Phys. Rev. B* **46** (1992) 14861.
- [95] Y. Zhu, Q. Li, Y. N. Tsay, M. Suenaga, G. D. Gu and N. Koshizuka // *Phys. Rev B* **57**(1998) 8601.
- [96] L. N. Bulaevskii, J. R. Clem, L. I. Glazman and A. P. Malozemoff // *Phys. Rev. B* **45** (1992) 2545.
- [97] J. E. Tkaczyc, R. H. Arendt, M. F. Garbauskus, H. R. Hart, K. W. Lay and F. E. Luborsky // *Phys. Rev. B* **45** (1992) 12506.
- [98] E. M. James, N. D. Browning, Y. Xin, J. L. Reno and A. G. Baca, In: *Proceedings of Microscopy of Semiconducting Materials IX*, Oxford, March 1999.
- [99] S. Rujiwarat, Y. Xin, N. D. Browning and S. Sivananthan // *Applied Physics Letters* **74** (1999) 2346.
- [100] Y. Xin, S. Rujiwarat, R. Sporcken, N. D. Browning, S. Sivananthan, S. J. Pennycook and N. K. Dhar // *Appl. Phys. Lett.* **75** (1999) 349.
- [101] R. Sporcken, M. D. Lange, C. Masset and J. P. Faurie // *Appl. Phys. Lett.* **57** (1990) 1449.
- [102] N. K. Dhar, M. Zandian, J. G. Pasko, J. M. Arias and J. H. Dinan // *Appl. Phys. Lett.* **70** (1997) 1730.
- [103] S. Sivananthan, X. Chu, J. Reno and J. P. Faurie // *J. Appl. Phys.* **60** (1986) 1359.
- [104] F. Wiame, S. Rujirawat, G. Brill, Yan Xin, R. Caudano, S. Sivananthan, N. D. Browning and R. Sporcken, In: *Proceedings of the 18th European Conference on Surface Science*, Vienna, Austria, September 21-24, 1999.
- [105] R. D. Bringans // *CRC Crit. Rev. Solid State Mater. Sci.* **17** (1992) 353.
- [106] Landolt-Bornstein, In: *Numerical Data and Functional Relationships in Science and Technology, Semiconductors* Vol 17. (Springer, Berlin, 1982)